An Overview of Technology Investments in the NASA Entry Systems Modeling Project

Michael J. Wright[‡]
NASA Ames Research Center, Moffett Field, CA 94035

Monica Hughes[§] and Anthony Calomino[†]
NASA Langley Research Center, Hampton, VA

and

Michael D. Barnhardt*
ERC Corporation, Moffett Field, CA 94035

The Entry Systems Modeling Project, within the NASA Game Changing Development Program, is in its third year conducting mid-TRL research in the disciplines of entry aerosciences and entry thermal protection materials. The Project team is working a variety of challenging problems ranging from the delivery of new aerothermal CFD codes, to the development of the first truly new ablation material response model in more than 40 years, to new conformal and truly flexible thermal protection materials, using novel polymer resins and advanced multi-layered concepts, that will revolutionize entry system designs for future NASA missions. This paper briefly summarizes the achievements to date of the ESM project and provides a full bibliography of papers published by the project over its first two years for the interested reader.

I. Introduction

Current planetary Entry, Descent and Landing (EDL) technologies are fundamentally limited in terms of landed mass and landing accuracy capabilities. The most challenging EDL problem facing NASA today is landing human crew, and the equipment they require, on the surface of Mars. Key technology challenges for this mission class were summarized by Braun and Manning.[1] In addition, NASA has conducted several conceptual system and configuration analysis studies of potential human Mars mission architectures. The most recent examples are the Mars Design Reference Architecture 5.0 (Ref. 2) in 2009, the Mars EDL Systems Analysis Study[3] in 2009-2010 and the current Human Spaceflight Architecture Team (HAT). The crux of the problem is that 1970s-era Viking heritage EDL technologies used for all Mars missions to date, including the Mars Science Laboratory,[4] are not extendable to payloads larger than about 1.25 t. The primary limitation is in deceleration of a large payload mass through supersonic speeds in the tenuous Martian atmosphere so that the terminal descent system has time to deploy and ensure a soft precision landing on the surface. Traditional parachutes, and the low lift over drag blunt aeroshells that deliver the spacecraft to the point of parachute deployment, simply will not scale to large payload mass. In order to enable landing of the larger payloads that will be required for large-scale science, in-situ resource utilization, and eventual human exploration, a new generation of innovative entry and descent technologies is required. Although current NASA plans do not call for human Mars exploration until the decade of the 2030s, the magnitude of technology advances that are required necessitate early investment in several (currently) low Technology Readiness Level (TRL) technologies. Flight tests in Earth's atmosphere and possibly at Mars will be needed in order to gain sufficient confidence in these systems before relying on them for a human expedition. Tracing back the schedule from human landing on Mars, assuming reasonable development times for the flight tests, and allowing for an

---

[‡] ESM Project Manager. AIAA Associate Fellow. Michael.J.Wright@nasa.gov
[§] ESM Deputy Project Manager
[†] ESM Materials Technical Area Lead
*ESM Aerosciences Technical Area Lead, AIAA Senior Member

occasional failure, it becomes clear that we need to begin such technology developments essentially now in order to meet the objective of humans on Mars in the 2030's. In addition, while human Mars exploration is certainly the grand challenge for EDL technologies, significant gaps exist for other destinations as well, including Venus, Giant Planets, and high velocity Earth return.

At the present time, most EDL related technology development efforts within NASA at the current time are contained within the Space Technology Mission Directorate (STMD). EDL investments in this Directorate range from system level architectures to component technologies, primarily at mid-TRL, with an expected maturity timeline of 2-3 years. Examples include the Low Density Supersonic Decelerator Project (LDSD), the Advanced Entry Placement Technology (ADEPT) Project, the Hypersonic Inflatable Aerodynamic Decelerator Project (HIAD), the Terrestrial HIAD Orbital Reentry (THOR) Project, the Thermal Protection System Materials Project (TPSM), and the Propulsive Decelerator Technology Project (PDT). In addition, a single project, Entry Systems Modeling (ESM), has a focus on lower TRL investments, primarily in the areas of Aerosciences and Thermal Protection Materials. This paper will discuss the background, requirements, and the status of current technology investments in ESM, which is currently starting its third year of execution.

II. ESM Project Objectives

The Entry Systems Modeling Project lies within the Game Changing Development Program (GCDP). The primary objective of the ESM Project is to develop enabling technologies and tools for hypersonic entry system design and development. The ESM Project includes foundational capabilities supporting the fundamental understanding of physics to enable or improve every NASA hypersonic entry vehicle. Additional technology development activities in the low-supersonic, transonic, and subsonic flight regimes are being considered in out-year plans to support the Descent and Landing portions of EDL. While most technologies for Low Earth Orbit (LEO) return to Earth, small payloads at Mars, and Earth sample returns are reasonably mature, those for the more ambitious missions planned by NASA in the coming decades are immature and require extensive development and testing.

The need for investment in EDL technologies is widely recognized within the Agency, derived in part from Strategic Goal 3.3 of the NASA 2014 Strategic Plan[5] to develop and demonstrate the critical technologies that will make NASA's exploration, science, and discovery missions more affordable and more capable. The NASA Office of the Chief Technologist (OCT) has acknowledged this need by identifying "High Mass Planetary Surface Access" as one of the 13 technology grand challenges for the Agency (December 2010). That document[6] states:

> "Entry, descent and landing is a challenging operation. A space system must be robust enough to accommodate a wide range of hazards associated with uncertain position and velocity knowledge, aerodynamic loading, atmospheric conditions, heating, particulates, and terrain characteristics to safely arrive at a desired surface location."

In addition, EDL was identified as one of the 14 key areas for which a technology development roadmap has been developed, again under OCT. Version 1 of the EDL technology roadmap (TA-09),[7] including comments and prioritization by the National Research Council (NRC) of the National Academy of Sciences, stresses the need for NASA to invest in the very near term in specific EDL technologies, with a total of seven technologies identified as high priority:

- Guidance, Navigation and Control (GN&C) Sensors and Systems

- EDL Thermal Protection Systems (TPS)

- Deployable Hypersonic Decelerators

- EDL Modeling and Simulation

- Instrumentation and Health Monitoring

- Atmosphere and Surface Characterization

- System Integration and Analyses

In particular, the top two scoring EDL technologies (GN&C and TPS) were selected as part of the top 16 crosscutting agency priorities for investment in the next five years. These technologies were noted to have broad,

potentially game changing benefit across a wide range of technology challenge areas. In addition, the NRC noted the importance of EDL modeling and simulation (M&S), and the NASA-uniqueness of the required technology development:

> "M&S tools are highly valued in every phase of design and analysis of EDL systems. In addition to development of physical models, numerical methodologies, and software tools to conduct M&S, this technology also includes development and application of experimental validation including flight tests. Only if high-fidelity models are also well validated can they be useful in reducing margins, thereby increasing mission capability without a loss in safety."

> "[NASA] currently possesses unique ground and flight test capabilities to conduct experimental validation required for EDL Modeling and Simulation. Continued investments in ground test facilities, such as large-scale wind tunnels, arc-jet facilities, and supersonic and hypersonic wind tunnels, will ensure that the means to validate codes are available when required. NASA is uniquely motivated to pursue this technology and major investments from industry are not expected in the absence of NASA involvement."

The investment priorities of the ESM Project are guided by these recommendations, with major technical focus areas in EDL modeling and simulation (aerosciences), TPS materials, and system integration. Version 2 of the OCT EDL Roadmap is under development at this time, and while some changes are expected, the overarching set of goals and objectives is likely to remain mostly unchanged. Of course, ESM priorities in future years will reflect any significant changes to the Roadmap as appropriate.

Initial technical products in the ESM portfolio were built on foundational work performed by the Aeronautics Research Mission Directorate (ARMD) Fundamental Aeronautics Program / Hypersonics Project (2006-2012), with a focus on near-term game changing advancements to the current state-of-the-art in key areas. Each task within the portfolio has a clear deliverable, achievable within 3 year timeframe, and one or more Key Performance Parameters (KPPs) that allow the Project and Program to assess performance toward meeting the stated deliverable. A clear focus of the initial portfolio is on the development, validation, and delivery of high-fidelity computational models for EDL aerosciences and TPS material performance. The successful delivery of these software products is determined by their validation, adherence to NASA software standards, and ultimately by their acceptance and adoption in the engineering design community. As such, the primary success criteria of the project from a software perspective are to deliver game changing improvements to the current state of the art in the physical fidelity and numerical efficiency of the simulation tools used to design NASA EDL Systems. The ultimate goal is to increase ease of use and facilitate early integration of high-fidelity simulation tools into the design environment. These improvements will translate directly to increased system reliability, robustness, and decreased design cost. The primary success criteria of the hardware elements are to deliver game changing materials and systems to NASA that will augment or replace the current state of the art, providing improved capability at increased reliability, lower mass, and/or reduced manufacturing cost.

A key aspect of the technical approach for ESM is to extensively leverage the support of stakeholders, and to continually seek direct and in-kind investment through innovative partnerships within NASA and with external partners. The project currently has multiple in-kind partners in three NASA Mission Directorates, three NASA centers, and Lawrence Berkeley National Laboratory. The project actively participates in the NASA Space Technology Research Fellowships (NSTRF) selection process, as well as the Early Stage Innovation (ESI) proposal calls. ESM staff are active in the EPSCOR process, and currently two Universities have active ESM-relevant EPSCOR grants. ESM is also involved in the SBIR/STTR selection process, and is seeking additional topic areas to better address EDL needs. Finally, ESM directly partners with Universities on several tasks.

The following sections discuss key technical products for the two main research areas of the Project: EDL Materials and Entry Aerosciences.

III. EDL Materials

The goal of the Materials area is to develop thermal protection system (TPS) materials and corresponding high fidelity models. Given the funding level of the project, the focus is on lower TRL concepts that can be matured to TRL 4 within 2-3 years and transitioned to another project for further maturation to TRL 6 and eventual mission infusion. Initial ESM materials investments include conformal ablators, flexible TPS, and high-fidelity ablation response models (including coupling of computational fluid dynamics to ablation response). The current status of each of these tasks is summarized herein.

A. Ablator Response Modeling

The objective of this task is to advance the state-of-the-art in ablative material modeling. The current state of the art of ablative material modeling remains codes derived from the Charring Material Ablator (CMA) code from the 1960's (Ref. 8). Analysis is typically conducted in one spatial dimension and assumes simple thermochemical equilibrium models for both the decomposition of resin and surface kinetic processes. While these codes tend to give conservative results of actual material performance, suitable for engineering design, they are inadequate for detailed analysis of post flight data from most NASA entry missions, which occur in a flight regime where nonequilibrium effects are important. Analysis of the data returned from the Mars Science Laboratory (MSL) Entry, Descent and Landing Instrumentation (MEDLI) project in 2012 highlighted these issues and demonstrated the need for new response models with higher physical fidelity.[9] It should be noted that the primary impediment to the advancement of the state of the art in material response modeling has been the perception in the community that validation of high fidelity models is not possible, and therefore it is pointless to include them in a simulation. It is this mindset that led this task to include a large experimental validation component, with a focus on innovative techniques to conduct component level validation of the new models being employed, supplemented with system level validation of the resulting codes using flight data from MEDLI and other sources.

Initial efforts have been focused on low-density carbon/phenolic composites, with a specific emphasis on Phenolic Impregnated Carbon Ablator (PICA), given its extensive use by NASA for resent and planned missions. As the modeling of low-density carbon-phenolic becomes mature enough to allow technology/expertise transfer, investigations into other materials will gradually be initiated. The modeling strategy follows three interdependent thrust areas: (1) develop a general-framework volume-averaged physics-based model and implement the overall model in a research computational platform, verify the tool, and run sensitivity analyses with theoretical materials properties, (2) independently develop for each phenomenon detailed physics-based models for real materials, (3) carry-out and coordinate component validation studies focused on key physical models.
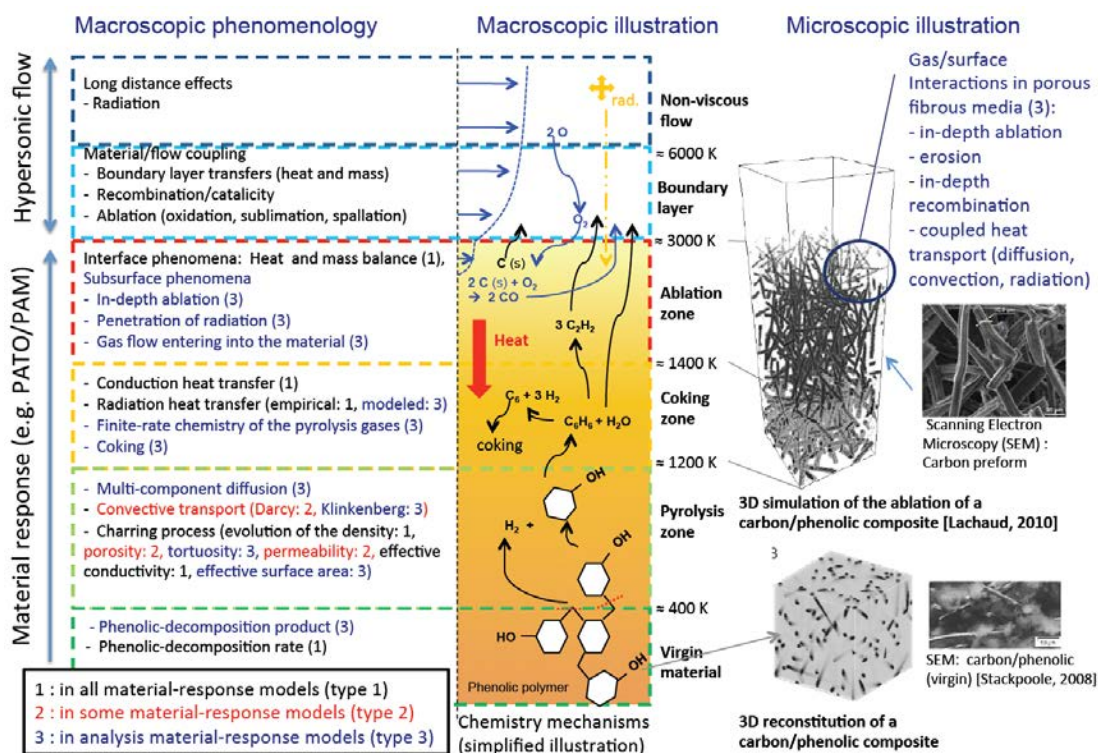

Figure 1. Ablative response of a low-density carbon/phenolic composite.[10]

A conceptualized volume-averaged mathematical framework of a multi-scale model for low-density carbon/phenolic ablators is shown in Fig 1.[10] This model is being implemented in a new material response code that is specifically designed to enable easy model development and analysis: the Porous material Analysis Toolbox based on OpenFOAM (PATO).[10] PATO is a fully portable OpenFOAM library written in C++. As compared to current

state-of-the-art models (denoted as Type 1 in Fig. 1), the following additional volume-averaged conservation equations have been incorporated in PATO: non-pyrolyzing solid mass conservation (in-depth coking and ablation), species conservation including multi-component diffusion in finite-rate chemistry conditions, momentum conservation in porous media (via Darcy's Law) using accurate gas (viscosity) and geometrical properties (tortuosity and permeability), and upgraded energy conservation. In a more recent upgrade,[11] volume-averaged element conservation including multi-component diffusion in equilibrium chemistry mode was added to allow modeling accurately arc jet test samples under the conservative equilibrium assumption (allowing boundary layer gas flow within the sample and mixing with pyrolysis gases). PATO is now the most advanced research code for the implementation of high-fidelity ablation response models. Verification and validation of PATO is ongoing, with sample cases developed in conjunction with the NASA/AFOSR Ablation Workshop series.

The task also undertakes, oversees and collaborates on a series of component model validation experiments conducted in house, at Universities across the country, and other national laboratories. At the current time the ESM project is managing active collaborations with grantees in the NASA EPSCOR program, Space Technology Research Grants program, Space Technology Research Fellowships, Early Stage Innovation program, and with Lawrence Berkeley National Laboratory. A summary table of the experiments/actions in progress is available, and can be provided upon request. The remainder of this section briefly highlights some of these studies; see Refs. 10-18 for more detail.

A model for the decomposition of phenolic resin has been implemented into PATO, and the importance of accounting for finite rate chemistry effects has arguably been demonstrated.[10] In order to determine the elemental and molar composition of pyrolysis gases, batch reactor experiments have been carried out. The experimental setup shown in Fig. 2a was used to study the decomposition of a generic polymer and to quantify gas species production by state-of-the-art gas chromatography analysis.[14]
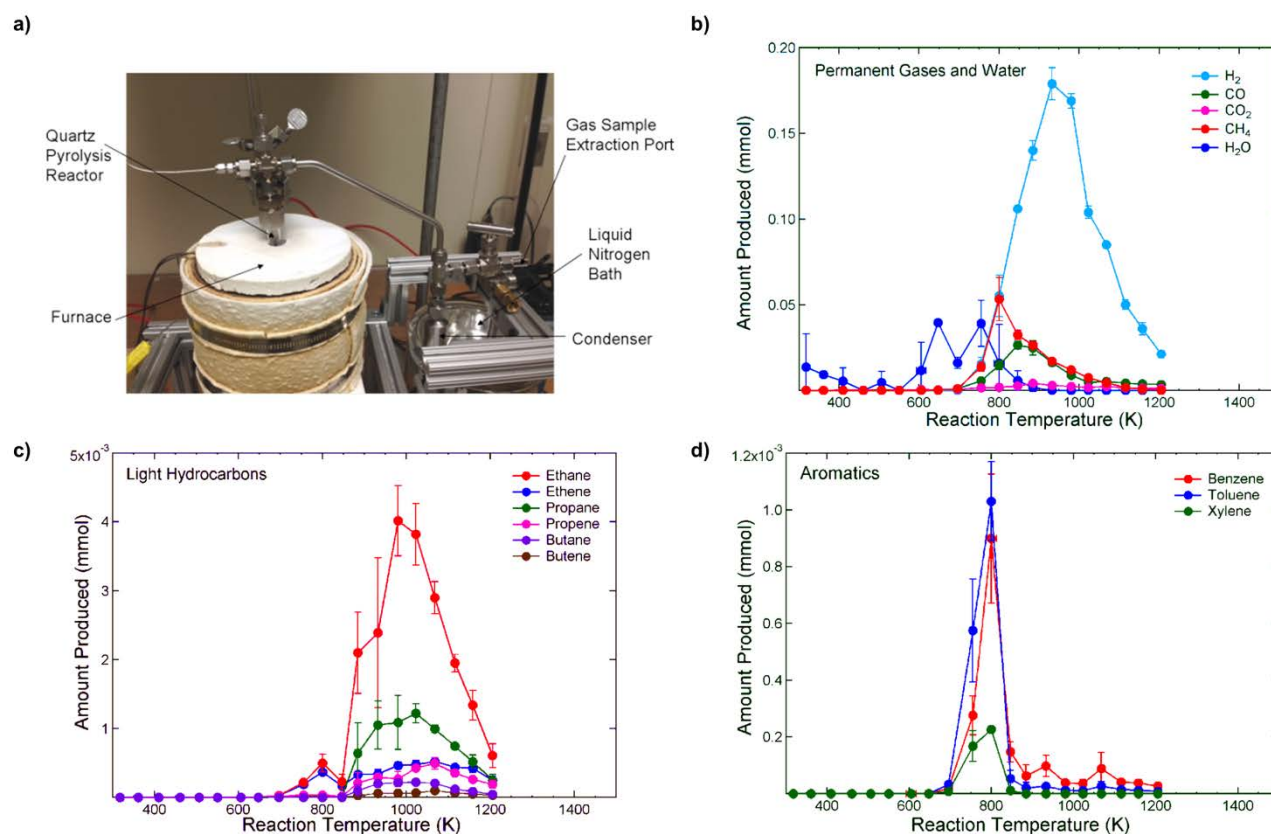

Figure 2. a) The Aerodyne batch reactor system for phenolic decomposition experiments. b-d) Amount of pyrolysis products measured using gas-chromatography.[14]

From the analysis of phenol-formaldehyde decomposition products, presented in Fig. 2b-d, the following conclusions are drawn:

1) Water is the main product below 800 K
2) Light hydrocarbons have peak production at 1000 K
3) Aromatic products are produced between 700 and 850 K

Analysis of liquid products from these experiment will be presented in a forthcoming publication.[17] The ablator response model activity has also recently concluded a series of elemental decomposition experiments using PICA samples,[18] and is finalizing the design of an upgrade to the reactor setup that will enable the study of the coking phenomenon and the finite-rate chemistry of pyrolysis gases flowing through high temperature carbon preform. The upgraded reactor is currently being manufactured.

The modeling of heterogeneous chemistry is a key feature for physics-based simulations of carbon/phenolic ablators. Characterizing the decomposition of carbon fibers in the presence of oxygen is needed to derive heterogeneous reaction rates used as input to the mass conservation equation for the solid phase. A preliminary validation effort, dedicated to determining the effective fiber reactivity, has demonstrated the capability of PATO to predict surface recession of Fiberform.[10] This study covers temperatures from 700 to 1300 K and pressure between 1.6 and 60 kPa and spans two experimental campaigns performed in the flow-tube reactor facility at NASA Ames. A first campaign has been conducted using hollow cylindrical FiberForm samples inserted in the test section of the tubular reactor.[13] The test gas (air) was flown through the hollow samples, progressively ablating their inner walls. A second campaign used full cylindrical samples that plugged the side-arm tube, forcing the flow to percolate through the porous medium.[15] The performed studies led to the following observations/conclusions.

1) Oxidation decomposition of carbon fibers manifests in the form of a pitting of the fiber surface that weakens the fiber structure (see Fig. 3, from Ref. 13)
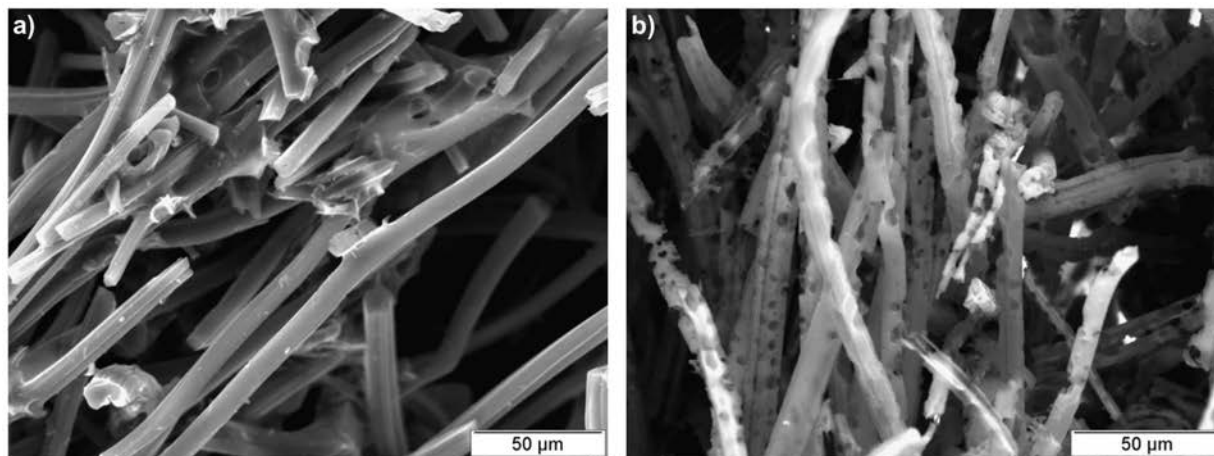

Figure 3: Scanning electron micrographs of a) virgin and b) oxidized FiberForm.[13]

2) Impurities detected in Fiberform can act as catalyzing agents for C-fiber/O_2 reactions enhancing oxidation and accelerating the decomposition of the material.
3) Thiele number analysis showed that most of the oxidation processes in flow-tube reactor conditions occur in a reaction limited (volume ablation) regime. This suggests the need to determine in-depth material properties as a function of oxidation, especially density profiles.

In order to address the lack of high-fidelity three-dimensional information on the fibrous architecture of carbon/phenolic ablators, the Project introduced the use of synchrotron X-ray microtomography to study highly porous heat shield materials.[12,16] Over the past two years we have collaborated with the Advanced Light Source (ALS) beamline at the Lawrence Berkeley National Laboratory synchrotron facility. The use of a synchrotron X-ray source has resulted in 3D images of the fibrous structures carbon/phenolic materials with micron-scale resolution,

low noise and very high quality. An example of image rendering, rebuilt from ALS data, is presented in Fig. 4 for FiberForm and Mersen CALCARB CBFC, used as structural materials for PICA and PICA-X (the Space-X variant of PICA) respectively. The images reveal detailed features such as hollow fibers for FiberForm (not known prior to this work) and the presence of fiber clusters and bundles for both materials. More recently, X-ray tomography of PICA has demonstrated the ability to image not only the fibers, but also the void filling phenolic resin. Tomography experiments have also been conducted in support of the CA-250 conformal and HEEET woven TPS products in the TPSM Project.
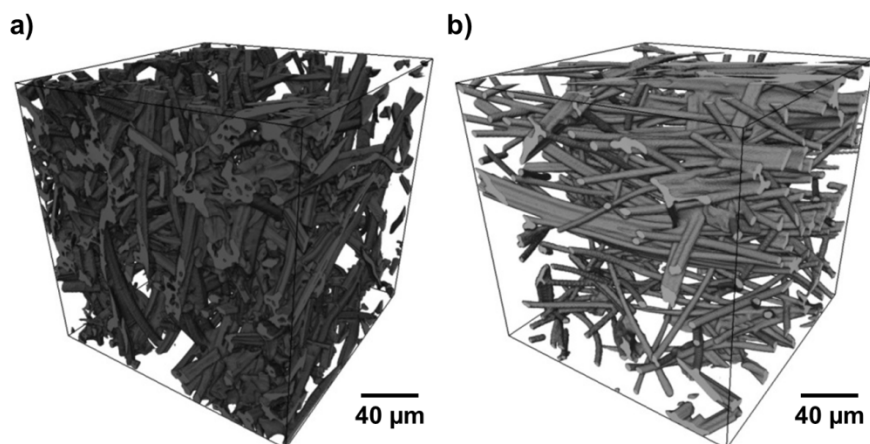
Figure 1. Volume rendering of a 1000³ voxel tomography of a) FiberForm and b) CALCARB. Pixel size is ≈0.325 µm in each image.[16]

In addition to providing direct insight into the internal structure of ablators, the microtomography images are also used to estimate quantitative material properties for high fidelity modeling such as specific surface area, tortuosity, and porosity.[12] Figure 5a shows the distribution of surface area versus the grey-scale level of each voxels within a microtomography image. The resulting image is rendered as "solid" or "void" using a cut-off value range to differentiate between the two. Once it is known where in the volume the voids are, quantities such as tortuosity (Fig. 5b) can be computed via statistical analysis. The recent acquisition of GEODICT software is expected to greatly facilitate the evaluation of material parameters from such datasets.
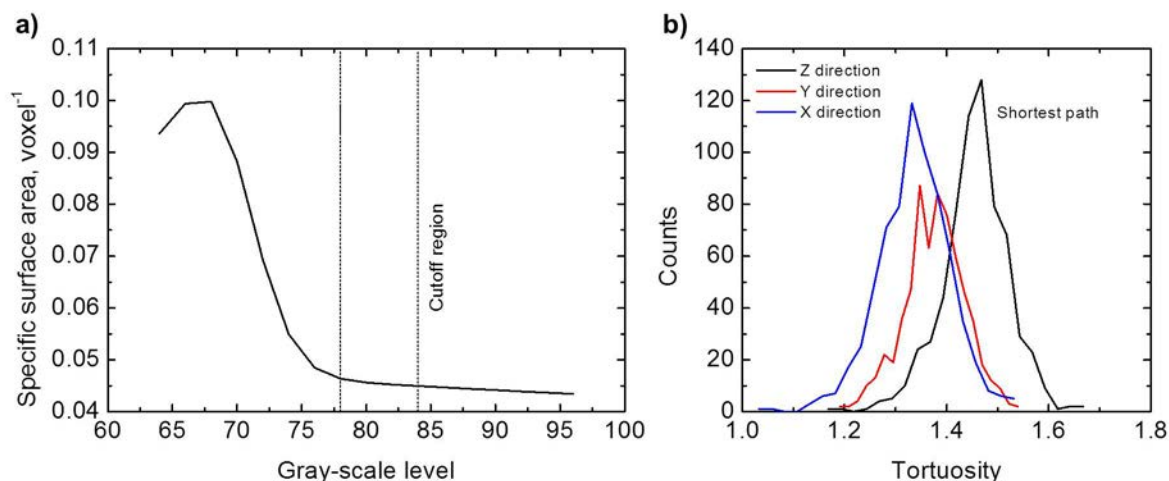

Figure 2: a) Specific surface area of carbon fibers as a function of the gray-scale cut-off, and b) distribution of the shortest path from one side of the FiberForm volume to its opposite side, computed using a cut-off pixel value of 80 (Ref. 12).

One focus of the microtomography work is to analyze PICA, FiberForm and AQ61 samples in their virgin state and others that have been extracted from test models oxidized in the Ames flow-tube reactor facility (in both air and CO_2) and that have been exposed to high enthalpy plasma testing. This will allow the evaluation of changes in material properties as the materials decompose. Results from this work have not yet been published, but will be presented in upcoming papers.

In order to handle the large datasets (~1 gigavoxel) generated from X-ray microtomography, we have started the development of a computational platform for the analysis of tomographic datasets and for performing numerical simulations of material and flow properties called the Porous Material Analysis (PuMA) toolbox. PuMA is currently able to import tomography data or internal generate a representative fibrous geometry, perform basic image processing to assist in 3D rendering, and compute statistics-based material properties as surface area and porosity (Fig. 6a). PuMA has also been implemented in a simulation library that is able to model the microscale oxidation of carbon fibers using a sticking probability technique for the surface oxidation reactions and a marching cube algorithm for tracking the fiber recession, similar to that proposed in Ref. 19. Figure 6b shows an example of a microscale surface ablation simulation of FiberForm, in which the fibers near the surface (top of the figure) have thinned due to oxidation. Results from this new simulation capability will be shown in a future paper.
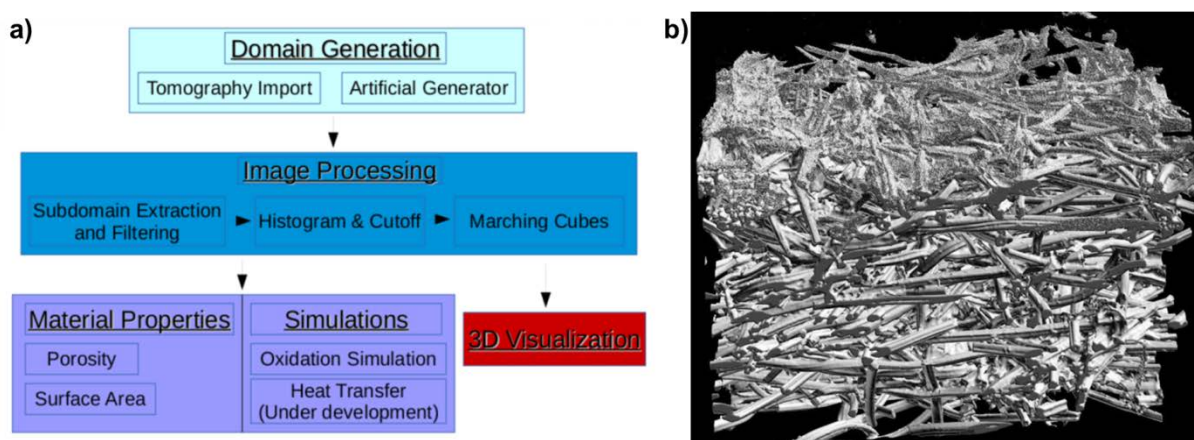

Figure 6. a) Schematic of the current PuMA structure and b) Tomography-based PuMA simulation of the surface oxidation of FiberForm.
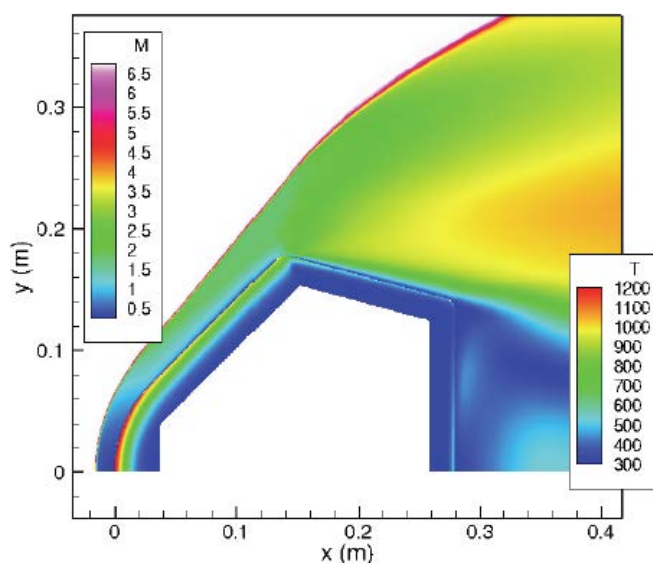

Figure 7. DPLR-ARM simulation over SPRITE geometry.[22]

Finally, a new effort began in 2014 to develop an engineering ablation response model (ARM) based on the data structure and solution algorithms inside the Data Parallel Line Relaxation (DPLR) code.[20] As a first step, only thermal conduction was modeled, with the intent of expanding the capabilities to include full ablative material response. The material response equations were implemented within the DPLR framework to produce a structured solver and applied to compute the coupled fluids-material response simulation over the Small Probe Reentry Investigation (SPRITE) geometry[21] at Mach 7.1 conditions representative of an arc jet test.[22] Figure 7 shows a snapshot of the coupled simulation showing Mach number contours in the fluid domain and temperature contours in the solid domain. Although the preliminary results were promising, the work clearly demonstrated the difficulties inherent in adapting an existing code and set of data structures to an entirely new set of governing equations and integration procedure. As a result of this work, as well as the success demonstrated by coupling independent codes via the libMesh framework (see next section), it was decided to stop development of the DPLR-ARM and focus on a new standalone engineering ARM beginning in 2015.

B. Ablator Response CFD Coupling

CFD-ablation response coupling has been attempted by many previous authors, and results have been presented for multiple geometries, typically using a loosely coupled approach in which the steady state CFD solution is used to drive a material response calculation, the results of which are fed back into the CFD. The objective of this effort was to obtain a tighter degree of coupling, and to do so in a way that would be generally applicable to many available CFD codes and ablation response models. In order to facilitate a standardized data transfer process, the C++ library tool libMesh[23] was chosen, and coupling was demonstrated using libMesh between three different CFD solvers and the CHAR[24] and TITAN[25] ablation response codes.

As a first step, the CFD code FINS[26] was coupled to CHAR,[27] completing work that had begun prior to the beginning of the ESM project. This code served as the pathfinder application and demonstrated the utility of the libMesh C++ library. DPLR was then converted from a standalone executable into a callable subroutine. The mesh-free interpolation routines from the libMesh libraries were incorporated into the code to pass boundary data between DPLR and CHAR. Initial development was performed on a two dimensional version. A central "handler" code was developed to run DPLR and CHAR in an iterative manner and facilitate boundary data transfer between them. The coupled DPLR-CHAR code was applied to a conduction-only problem over a 45° sphere cone with a freestream velocity of 5.92 km/s. The solid body consisted of an external layer of copper on top of a layer of aluminum. The DPLR-CHAR results were then compared with FINS-CHAR. Temperature contours through the shock layer and solid are shown in Fig. 8. The in-depth temperature contours are in good agreement, indicating proper implementation of the boundary data transfer in both codes. The differences in the solid temperature contours are due to slightly different surface heating rates computed by *DPLR* and *FINS*.[28]
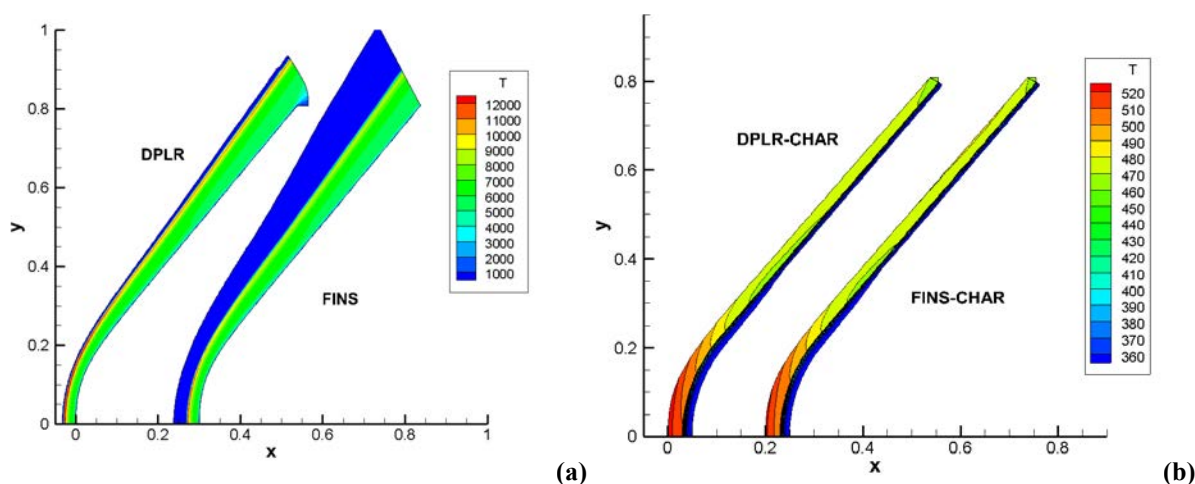

(a)   (b)

Figure 8. Temperature contours through the fluid (a) and solid (b) comparing DPLR-CHAR and FINS-CHAR results.[28]

Next, DPLR was coupled to the TITAN code,[29] a 2D/axisymmetric ablation response solver. The coupled code was applied to arc jet flow over an iso-q geometry constructed of PICA. The DPLR-TITAN results were compared against previous TITAN values and against arc jet experimental data on surface recession rates. Figure 9 shows

temperature contours in both the external flowfield and inside the solid iso-q geometry after the model had been exposed to the flow for 27 seconds. The coupled DPLR-TITAN code predicted the surface recession rates to within 8% of the experimental measurements.[28] The DPLR-CHAR implementation has since been extended to fully three-dimensional simulation; results will be presented at a future conference.
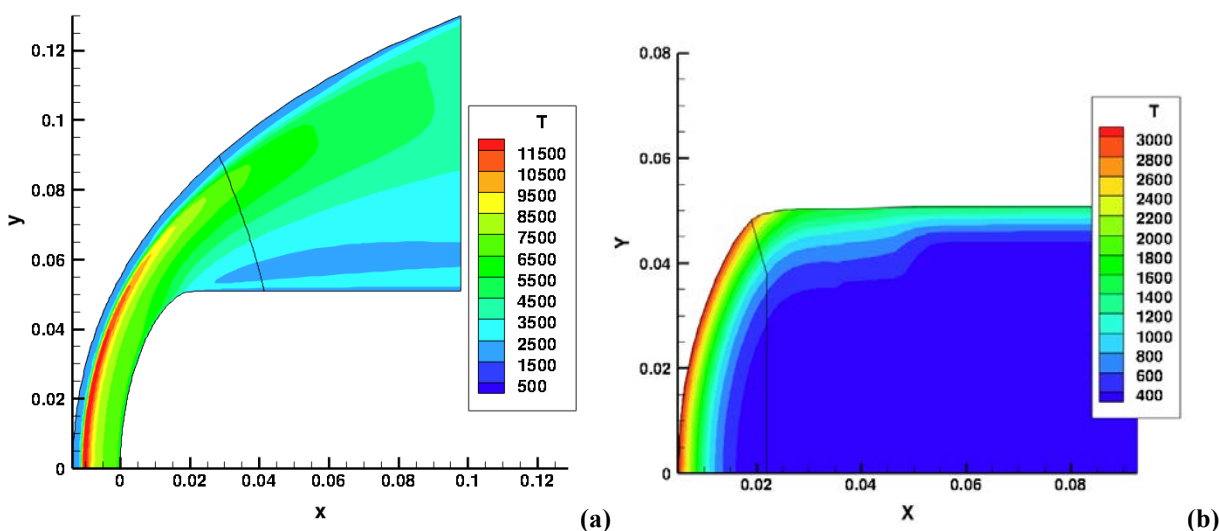

Figure 9. Temperature contours for iso-q simulations, (a) External flow, (b) Solid temperature contours.[29]

Most recently, the FUN3D code[30] has been coupled with CHAR through the same libMesh formulation, and tested on a problem with includes both material response and radiation coupling (via the HARA code[31]). In this multi-physics simulation, FUN3D provides a total heating rate and surface pressure to CHAR and shock layer profiles of species densities and temperatures to HARA. HARA provides the radiative heating and radiation source terms for the energy equations in FUN3D. CHAR calculates the temperature distribution and shape change due to TPS ablation and changes to the structure of the vehicle as a function of time. It also provides the surface temperature and species mass loss rate from the TPS as a boundary condition for FUN3D. This feature enables a more comprehensive simulation capability and model sensitivity analysis required for uncertainty quantification. Figure 10 shows an early result of time dependent energy soak into a simplified capsule structure for the Multi-Purpose Crew Vehicle (MPCV). In this simulation at 6.35 km/sec, the structure temperature and convective heating rate evolves in time, showing effects of conduction but not ablation or radiation. A users manual describing the FUN3D-CHAR coupling will published as a NASA Technical Memorandum.
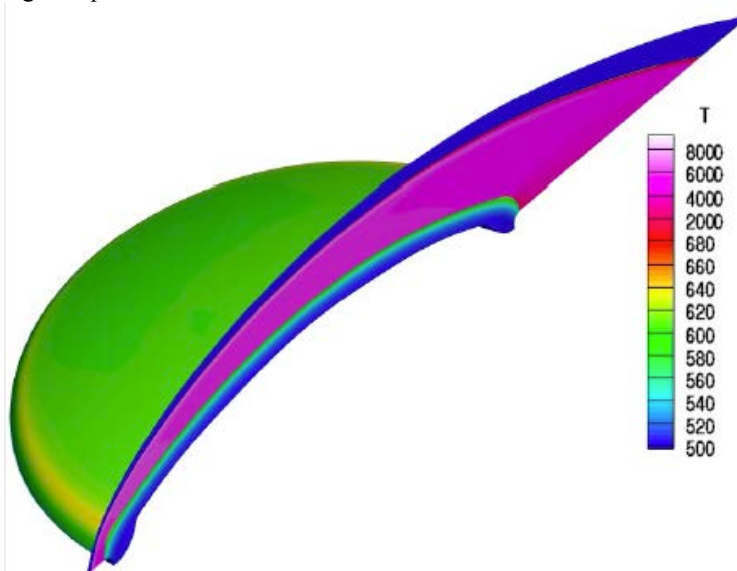

Figure 10. Temperature soak into the MPCV heatshield at 6.35 km/s.

The results presented here demonstrate that, via the libMesh framework, it is straightforward to establish a tight coupling between material response and CFD. At the current time a total of three CFD codes and two material response codes have been coupled, and it is expected that future material response codes, such as PATO and the engineering ARM under development will be readily coupled to existing CFD codes as desired in the future.

C. Advanced Ablative TPS

A conformable TPS over a rigid aeroshell has the potential to solve a number of challenges faced by traditional rigid TPS materials (such as the tiled PICA system on MSL or the honeycomb-based Avcoat on the Orion MPCV). The compliant (high strain to failure) nature of the conformable ablative materials facilitates integration of the TPS with the underlying aeroshell structure and enables monolithic-like configurations where large acreage segments and consequently fewer parts can be used. The high strain to failure nature of conformal ablators significantly increases the vehicle-TPS design space by allowing for integration on a wider range of carrier structures and the ability to accommodate changes to the substructure late in the design phase without detriment to the overall TPS design.

First developed as the Conformal 1 ablator under the Hypersonic Project in the early 2000s, conformal ablators have demonstrated superior integrated heat load capability failure strain tolerance as compared to conventional PICA at comparable bulk density. This material concept replaced rigid FiberForm with a conformal carbon felt as the substrate, but retained phenolic as the resin, and used modified PICA processing techniques. As such, the material is colloquially known as "conformal PICA." Given the potential benefits, the Conformal 1 ablator served as the starting point for the GCDP Project element CA-250, which has since improved and matured the concept to a TRL of 5. However, the Conformal 1 concept was essentially envisioned as a baseline point solution to a new family of TPS, which ESM seeks to broaden by looking at:

1)   alternate felt substrates with improved physical and mechanical properties
2)   alternate resins with enhanced mechanical, physical and decomposition properties
3)   computational materials modeling to support the experimental tasks

Alternate felt substrates was explored under the first phase of the research effort primarily to reduce surface recession rate as the baseline Conformal 1 ablator demonstrated significantly higher ablation recession than PICA due to the spallation of poorly interlocked fibers. In order to understand its influence, the degree of carbon fiber interlocking was studied through the use of a variety of felt systems and commercially available needling capabilities, which led to a down selection of two alternate carbon fibrous substrates that were compared to the baseline Morgan felt system used in Conformal 1: a polyacrylinitrile (PAN) based system and a rayon based felt system. The overall goal of the first phase of study was to identify a substrate fiber material, needling requirement, and fiber load density together with a resin loading that would reduce spallation for improved ablation resistance without sacrificing either strain tolerance or integrated heating performance.
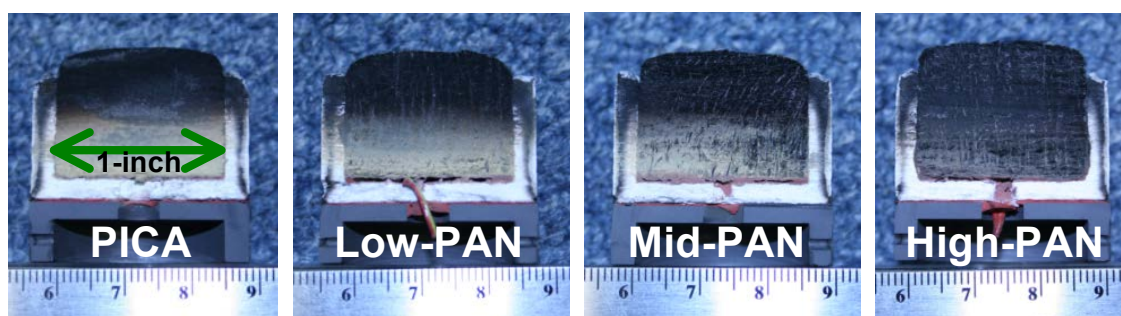

Figure 11. Cross-sectional view of PICA, Low- Medium- and High-density PAN HyMETS test articles.

In order to effectively explore the option trade space, test samples with a high and a low fiber loading produced with differing needling requirements were fabricated with at two resin loadings for both the PAN and rayon based systems. The test samples were then screened under simulated aerothermal re-entry conditions at the HyMETs facility at NASA LaRC. Results from the HyMETs thermal exposure test are shown in Fig. 11 for the various PAN options. Following the thermal screening tests, a down selection of the most promising material was made for further evaluation in the Interaction Heating Facility (IHF) at NASA Ames planned for January 2015. Initial testing will be performed in stagnation at a heat flux of approximately 1200 W/cm^2, and second series of tests will be at a lower heating level of 400 W/cm^2 using a novel SPRITE test configuration that will expose multiple materials to

shear flow. An assembled SPRITE model for one of these tests is shown in Fig. 12. The results from IHF testing will be used to quantify improvements made to the ablation resistance due to fiber substrate and resin loading changes.
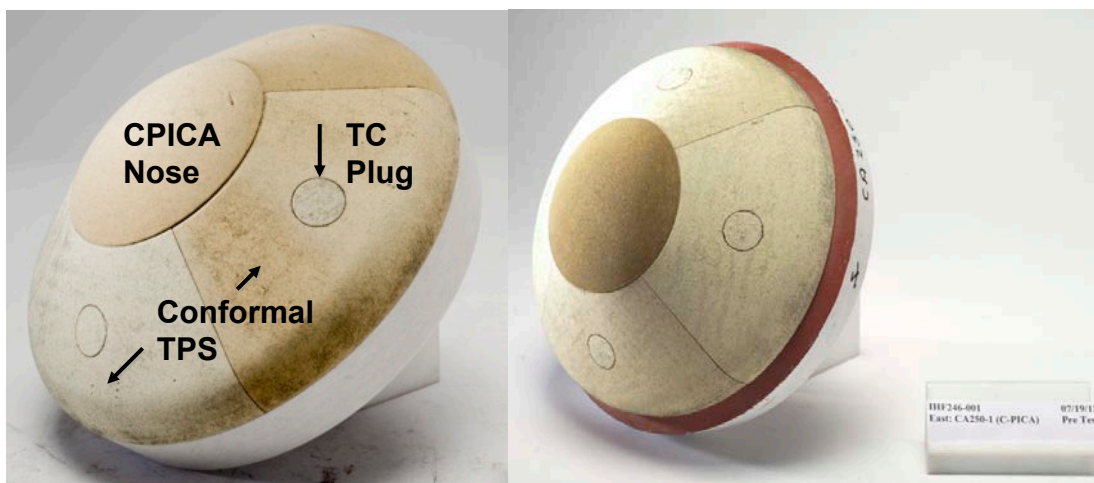

Figure 12. Fabricated SPRITE models for IHF testing.

The second parametric consideration in the trade space for improving the performance of conformal ablators is the resin chemistry used to infiltrate the felt substrate. Although phenolic is the legacy resin choice for ablative TPS, there are other organic resin chemistries that have the potential to enhancing strain properties, improve thermal decomposition kinetics, yield more char, shorten process time, and/or provide a "greener" manufacturing process.[32] The second phase of the ablator material is to investigate the benefits of alternate resin chemistries. However, a primary difficulty to exploring this trade space is discovering the solvents and processing requirements needed to uniformly infiltrated a resin into the substrate and cure it such that it develops a void-filling "fluffy" structure characteristic of phenolic in PICA as shown in Fig. 13. Three resin chemistries are under consideration: cyanate-ester, pthalonitrile, and polyimide. Current work is focusing on developing conformal TPS samples with some or all of these resins using the down selected felt substrates from Phase 1. The results of this work will be presented in a future paper.
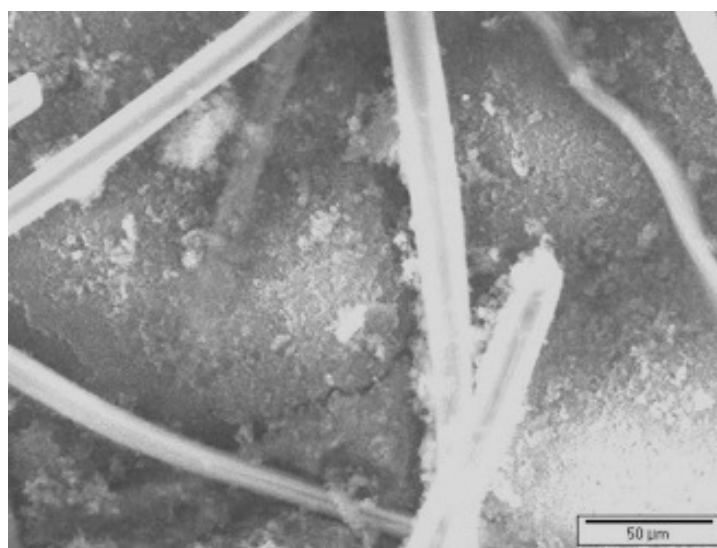

Figure 13. SEM image of conformal PICA showing the carbon fibers and high surface area "fluffy" phenolic filling the voids.

The final part of this task is a computational materials effort, intended to guide the research into tailored TPS materials. Some key results from this modeling work are presented in Refs. 33-35.

The long-term goal of the Advanced Ablators task involves the development of novel ablative TPS materials for missions with peak heating from 250 to greater than 1000 W/cm^2, a range of heat fluxes that should make these systems attractive for a range of missions ranging from MPCV extended capability, science and exploration Mars missions, and Earth return of samples or crew. Further exploration of the option space of the conformal ablator family, together with the successful maturation of the CA-250 materials as a point example in this space, have demonstrated not only the potential utility of conformal systems for a range of possible NASA applications, but also the feasibility of maturing the system with the right properties for a given mission application in a relatively rapid timeframe.

D. Advanced Flexible TPS

The successful flight of the Inflatable Re-entry Vehicle Experiments (IRVE)[36] has demonstrated the feasibility of using a hypersonic inflatable aerodynamic decelerator (HIAD) for planetary entry. However, successful mission infusion of this technology requires a thermal protection system that is capable of surviving the aerothermal loads while maintaining a durability and flexibility that provides for the rigors of manufacturing, handling, packing, stowage and deployment. To address those challenges, NASA is investing in the development of Flexible Thermal Protection Systems (F-TPS). Under a separate technology investment effort funded by the NASA STMD GCD Program, the HIAD project made use of commercial materials available at high TRL to advance its Generation-1 F-TPS to a 30-40 W/cm^2 cold wall heat flux capability and its Generation-2 F-TPS to a 50-60 W/cm^2 cold wall heat flux capability. The HIAD project advanced F-TPS technology to a flight readiness level using commercial materials and successfully flew the Generation 1 thermal protection system on the IRVE 3 vehicle.[36] In concert with these developments, the ESM project is focused on lower TRL investments in F-TPS materials and material systems technologies that are capable of extended performance beyond 60 W/cm^2. Current systems studies for crewed Mars missions anticipate an F-TPS heat flux capability of 75-100 W/cm^2 cold wall heat flux will be required for eventual exploration class human missions that use HIAD technology. In order to achieve this capability, candidate heat shields must be high temperature capable systems that are reliably deployable and offer excellent packing efficiency and handling resilience.

The objective of ESM F-TPS investments is to develop innovative high temperature insulator materials from an emergent laboratory capability to a TRL 4+ technology that will reduce overall heat shield mass and volume requirements while improving peak heating and integrated heat load capability. The fundamental engineering approach underlying the F-TPS design is a modular, multi-layered system consisting of a silicon carbide refractory textile outer layer that accommodates peak heating and aero-pressure loads. The refractory textile overlays layers of insulators designed to manage integrated heat load such that the gas barrier temperature remains below its performance limit. The entire system, including the impermeable gas-barrier, must accommodate being packed into a stowed configuration for launch and cruise. The technology maturation path is to develop three classes of flexible TPS: a 50 W/cm^2 system, a 75 W/cm^2 system, and a 100 W/cm^2 system (all cold wall values). In September of 2013, the ESM project delivered a 50 W/cm^2 F-TPS solution that is both lighter and more capable than the HIAD Generation 2 F-TPS system. Development of the 75 W/cm^2 and 100 W/cm^2 systems are following a standard process whereby screening tests will be used to inform material down-selects and subsequent thermal properties testing that eventually forms a baseline configuration.

Insulator material investments encompass both inorganic and organic systems. These systems cover the spectrum from passive non-decomposing insulators to actively decomposing materials that offer the benefit of endothermic gas reactions and transpiration cooling (analogous to the pyrolysis process in an ablator). Insulators are designed to meet the functional requirements of a modular layup. Heat transfer immediately below the refractory textile is dominated by thermal radiation transfer, so advancements for insulators located in regions exposed to extreme temperatures include radiation inhibitors (opacifiers) that diffuse and re-reflect infra-red radiation, as shown in Fig. 14a for the Opacified Flexible Insulator (OFI)-2 system. Material developments for lower insulator layers are designed to impede heat transfer through gas advection. This is primarily accomplished with the development of inorganic aerogels impregnated in a refractory fibrous mat, shown for the APA-2AS insulator in Fig. 14b, for the higher temperature regions located just beneath the radiation transfer zone, and organic aerogel systems, for example the polyimide films shown in Fig. 14c that are effective at cooler regions just above the gas barrier. Manufacturing techniques that improve packing and handling properties are included as part of the technology development activity. These techniques include scrim backing, needling, texturing, and bonding.
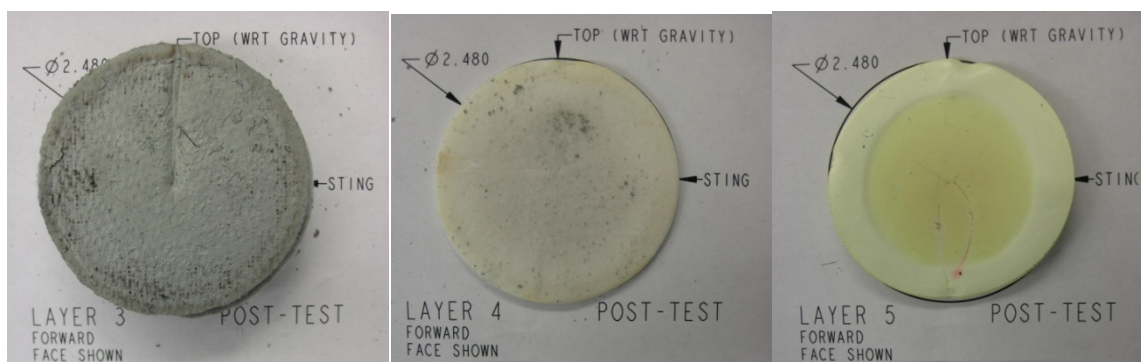
Figure 14. Functionalized TPS insulators designed to improve resistance to a) radiation, b) high temperature gas advection, and c) moderate temperature gas advection.
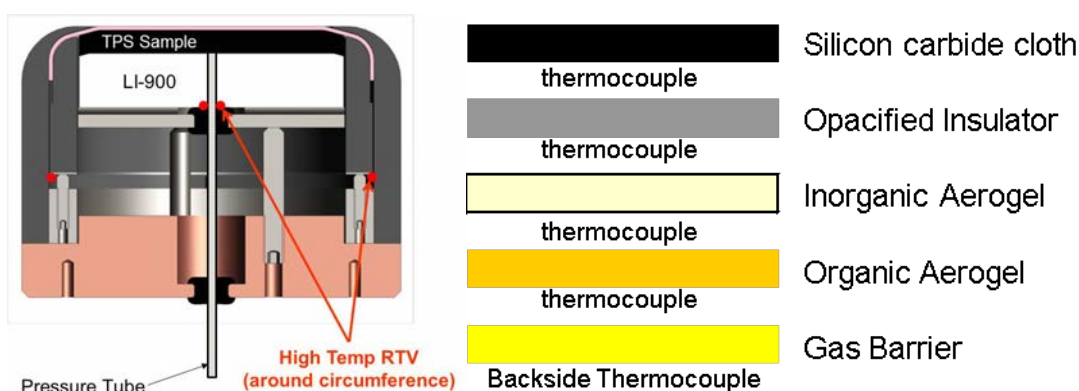

Figure 15. a) Flexible TPS sample holder used to perform arc jet stagnation testing, and b) Typical modular configuration for a flexible TPS, showing locations of thermocouples.
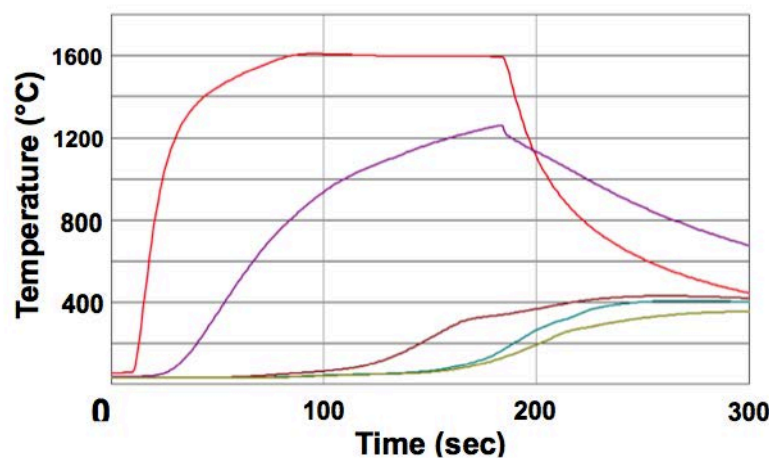

Figure 16. Temperature measurements on the 50 W/cm^2 F-TPS layup configuration tested at LCAT.

The performance of each material system is optimized to best meet the functional requirements of the targeted layer based on the expected operational temperature and dominant thermal transfer mechanism of the modular F-TPS configuration. The integrated F-TPS stackup is then assembled as one or more layers of each type of material, with the final stackup dependent on mission requirements. The thermal performance of the modular F-TPS configuration in both stagnation and shear heating environments is assessed from fixed heat flux thermal exposure tests performed in the Boeing Large Core Arc Tunnel (LCAT) facility using specialized F-TPS stagnation test

sample holders to hold an instrumented TPS stackup as shown in Fig. 15. Typical experimental measurements acquired during testing are thermal transfer time histories within each insulator layer as shown in Fig. 16. Thermal tests provide comparative performance metrics between various insulator developments and modular F-TPS configurations, as well as absolute performance metrics against ESM program goals. More information on details of the F-TPS testing and analysis can be found in Refs. 37-40.

IV. Aerosciences

Entry modeling and simulation capabilities, including experimental validation, are a lynchpin of modern EDL design. Ground test limitations generally preclude a "test as you fly" approach to EDL systems, and flight tests are prohibitively expensive in most cases. As a consequence, validated high-fidelity models are used to extrapolate ground test results and to predict flight performance. The aerosciences technical area includes investments in three key thrust areas: improved CFD and Direct Simulation Monte Carlo (DSMC) simulation capability, shock layer radiation modeling, and aerothermal experimental validation. The following sections discuss the breadth of the ESM aerosciences portfolio.

A. US3D Development

In the area of CFD, the external aerothermodynamic environments of entry vehicles within NASA over the past two decades have been simulated with two independently developed codes. The Langley Aerothermodynamic Upwind Relaxation Algorithm (LAURA)[41] was first utilized in 1987 for simulations of a proposed Aeroassist Flight Experiment vehicle. The Ames Data Parallel Line Relaxation Code (DPLR)[20] has been utilized in parallel for defining vehicle entry environments since its use for Stardust and Huygens entry risk assessments in 2004. Both codes have been used for every NASA mission involving atmospheric entry since Mars Pathfinder, through to the present Orion/MPCV. Teams at Langley and Ames have benefited over the years by the ability to cross check, verify and improve the independently developed algorithms and physical models used in the two codes. In fact, given the uncertainties in extrapolating ground test data to the flight environment, having two independently developed codes for aerothermal simulation is both prudent considered necessary. However, some recent advances in aerothermal modeling, notably those involving unstructured grid formulation, have not been incorporated into these tools, due in part to their software architectures. Unstructured grid algorithms offer greater flexibility than block structured approaches (even with the use of overset gridding) in both defining complex geometric features and in adapting the grid to the shocks, expansions, and free shear layers endemic to hypersonic flow. The Hypersonics Project saw an opportunity to stimulate the development of next generation CFD software to augment and eventually replace both of these workhorse codes. The results of this effort, completed under the ESM project, are discussed in this and the following section.

The first new CFD code completed by ESM is Un-Structured 3D (US3D), developed for the simulation of compressible and reacting flows. The code has been in development for several years at the University of Minnesota, and had become established as a state-of-the-art aerothermal simulation capability.[42] In collaboration with the ESM project, US3D has now reached production-level maturity so that it can be used for large-scale simulations of a wide range of flows that are of immediate and future mission relevant to NASA.

US3D was designed as a next-generation extension of the widely used DPLR code. The principle difference between the two codes is the underlying unstructured mesh framework, which is chosen because of its advantages for geometrically complex problems. However, while US3D incorporates nearly all of the numerical and physical models of practical importance as its predecessor, US3D also has a number of capabilities beyond those available in DPLR. Among the enhanced features are: high order low dissipation numerical flux functions, turbulence models for wall-modeled large-eddy simulations, dynamic grid motion, uncoupled species equations to greatly reduce computational cost, and modular, application programming interface (API) architecture for easy, user-driven extensibility.

A distinctive feature of US3D is the availability of new high-order, low dissipation numerical methods[43] that emphasize resolution of fine, unsteady flow features. This feature enables US3D to perform very high resolution simulations of entry vehicle wakes, hypersonic boundary layers, and high-speed mixing characteristic of scramjet combustors, among other problems of interest. An example is shown in Fig. 17, which depicts the growth of boundary layer instability behind a discrete roughness element in a Mach 6 boundary layer at varying Reynolds numbers.[44] Seen in progression from top to bottom, US3D allows the Navier-Stokes equations to naturally resolve transition breakdown of the boundary layer as the Reynolds number increases. In a similar fashion, high order resolution of the unsteady wake behind a vehicle provides unprecedented insight into the aftbody aerothermal environment, as seen in Fig. 18 from Ref. 45. In addition to better vehicle heating estimates, when combined with a

moving mesh, such knowledge enables accurate simulation of the vehicle's dynamics.[46] This new capability, while not fully validated at the current time, has tremendous potential to augment or even replace the current experimentally driven practice where uncertainty is typically quite high due to facility limitations.
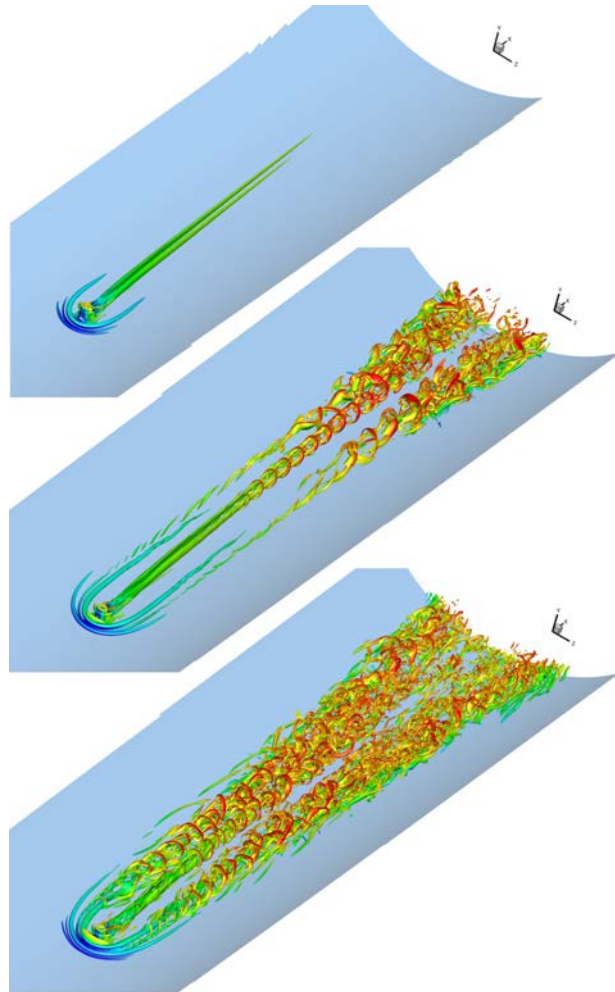
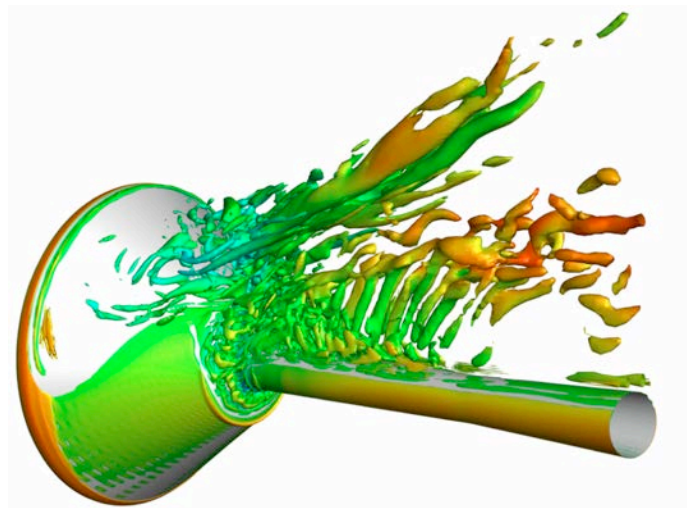**Figure 17: Simulation of discrete roughness in Mach 6 boundary layer at varying Reynolds numbers.[44]**

Figure 18: Visualization of vortical structures in the wake of a sting-mounted wind tunnel model.[45]

Another innovation of US3D is the ability to simulate reacting flow problems using a decoupled formulation for species mass conservation.[47] This approach reduces the size of the Jacobian matrix that must be factored, which in turn greatly reduces computational cost when a large number of species are present in the simulation. This reduction, while potentially reducing the overall stability of the system of equations, is of considerable importance when considering phenomena such as ablation of thermal protection materials where dozens of chemical species can be present in the flowfield.

In addition, utilizing US3D's API architecture, a user can modify US3D to solve material response equations coupled with the core Navier-Stokes module. This procedure was validated by Trevino & Candler through simulations of camphor sublimation, thermal response, and shape change.[48] Of special note is the ability of US3D to cleanly simulate recession using its moving mesh formulation without introducing spurious oscillations in the surface definition as the outer mold line recesses.

US3D was delivered in the middle of FY14 and is currently co-managed under the stewardship of the University of Minnesota and the Aerothermodynamics Branch at NASA Ames Research Center. See the companion paper for more detail concerning these and other aspects of US3D.[49]

B. Hyp-FUN3D Development

FUN3D is a node-based, fully unstructured, finite volume solver of the Navier-Stokes equations.[30] The baseline method uses least squares gradient information to execute second-order accurate inviscid flux reconstruction. A Green-Gauss formulation of gradients at the nodes is used for multi-dimensional reconstruction and calculation of viscous gradients across elements. The FUN3D code has undergone extensive development in the previous two decades for the simulation of flows across a wide speed regime ranging from incompressible to supersonic flow, but originally hypersonic flow simulation was not part of the tool for two reasons: the well known difficulty in properly capturing strong shock waves with an unstructured code, and the need for extensive physical models for non-equilibrium thermochemistry. The extension of FUN3D to hypersonic flow was again begun in the Hypersonics Project and completed under ESM. The extended capability code is called Hyp-FUN3D, or the generic gas path of FUN3D.

The baseline inviscid flux reconstruction algorithms in the generic gas path mimic those in LAURA, with adaptions for unstructured grids that greatly alleviate the well known difficulty in obtaining good solutions in the vicinity of strong shock waves.[50] As part of this work, FUN3D has also been modified to include the physical models used in LAURA for aerothermodynamic applications.[51] Indeed, both codes now share the exact same modules for thermodynamics, transport properties, chemical kinetics, thermal relaxation, and radiation. The test suites and user interfaces for aerothermodynamic simulation enable FUN3D to replace the functionality in LAURA, especially focused on problems supporting EDL applications. A critical element of this extension is documentation of the functional equivalence of FUN3D to LAURA for EDL applications. This functional equivalence has been documented[52] and an associated tutorial for use of the generic gas path through FUN3D is in review for publication as a NASA Technical Memorandum.[51]

A web-based regression test system is used that automatically checks for any impact of software changes to established functionality. FUN3D uses these established tests to confirm that its own functionality reproduces that of LAURA over a suite of test cases that touch most permutations of physical models, total energy, and geometric complexity of interest to the EDL community. These tests span perfect-gas, equilibrium, and thermochemical non-equilibrium gas chemistries representative of Earth, Martian, and Titan atmospheres. Axisymmetric and three-dimensional, blunt and slender configurations are included. In general, agreement with LAURA on identical grids and identical physical models is targeted to ±4% for surface pressure and heating.

Several capabilities in the current LAURA workflow have been reproduced in FUN3D and generalized to unstructured grids to encourage users to make the transition:

1. A "shuffle" utility was added that allows solution restarts from disparate physical models involving different numbers of governing equations. This capability utilizes a template in which new variables are initialized as needed, old variables are retained, and variables are eliminated if unused in the new model set.
2. An algorithm for identifying lines of nodes off the body to enable line-implicit relaxation, outer boundary alignment with the captured bow shock and the distribution of nodes in the boundary layer. This infrastructure has enabled implementation of coupled radiation and algebraic turbulence models.
3. Ray tracing from any point on the surface in any direction through the shock layer, which is required in situations where a tangent-slab approximation is not appropriate for analysis of radiative energy transfer to the surface.

An example of functional equivalence for a simulation including fully coupled radiative heating at the FIRE II (Ref. 53) 1643-second trajectory point (V = 10.84 km/s and ρ = 0.00078 kg/m^3) is presented in Fig. 19, from Ref. 54. Both CFD simulations used the HARA radiation code[31] and an 11-species, two-temperature thermochemical non-equilibrium gas model. Agreement between the two codes for convective and radiative heating is generally good. The line extraction capability described above is used to transfer radiative flux information between FUN3D and HARA assuming the tangent-slab approximation. Matching the radiative heating is simply a confirmation that the profiles of species densities and vibrational-electronic temperatures being passed to HARA from LAURA and FUN3D are in good agreement.
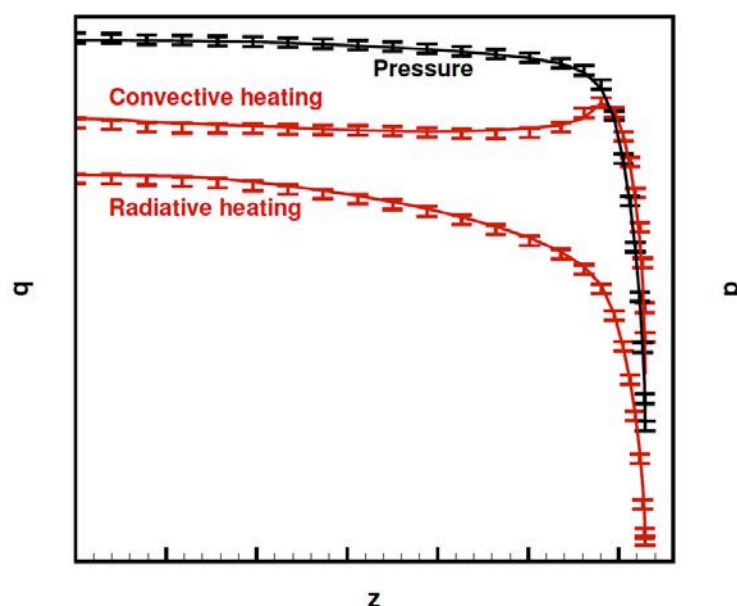

Figure 19. Comparison of convective and radiative heating between LAURA and FUN3D for FIRE II at 1643 sec. Lines are FUN3D. Bars are ±4% of LAURA.[54]

Hyp-FUN3D was delivered at the end of FY14 and is currently under the stewardship of the Aerothermodynamics Branch at NASA Langley Research Center. The latest users manual for the code (Ref. 55) includes information on running the generic gas path option, and the upcoming NASA TM (Ref. 51) will include a detailed tutorial. Future planned work on the code includes incorporation of Walsh function based flux reconstruction, which has the potential for game-changing improvements for the simulation of flows with strong shocks on unstructured grids. See Refs. 56-57 for more information.

C. DSMC Development

The direct simulation Monte Carlo (DSMC) method provides a probabilistic physical simulation of gas flows at a particle, rather than continuum, level. This method is very attractive for low density (more correctly high Knudsen number) flows, where the continuum assumption that is the basis of CFD breaks down. Technically, DSMC methods can be used for any fluid flow simulation, but because the cost of the simulation scales with the density (and therefore the number of particles), the use of DSMC methods in the continuum regime has been limited to date. The primary current application of DSMC methods within NASA are for the simulation of entry vehicles at high altitude, stationkeeping of objects in low orbit, aerobraking of spacecraft into planetary atmospheres, and thruster plume simulations in space.

Over the past decade, there has been much progress towards improved phenomenological modeling and algorithm updates for DSMC. These improvements allow for an expanded range of possible solutions in altitude and velocity space by increasing the numerical efficiency of simulation. However, NASA workhorse codes still lack significant important physical models, including proper treatment of ionization and shock layer radiation. NASA's current production code, the DSMC Analysis Code (DAC),[58] is well-established but is based on Bird's 1994 algorithms[59] and written in Fortran 77. In order to take advantage of modern programming practices, a new DSMC code is being developed in the C++ programming language using object-oriented and data-oriented design

paradigms to facilitate the inclusion of the recent improvements and future development activities. Current development efforts on this new code, the Multi-physics Algorithm with Particles (MAP), are summarized briefly here. For additional information please see Refs. 60-61.

Object-Oriented Design (OOD) has many advantages over conventional programming approaches. OOD provides a clear modular structure for programs and makes it easy to maintain and modify existing code as new classes can be created with relatively small differences to existing classes. Simply using OOD practices, however, can lead to random memory access patterns and constant cache misses, which degrade the computational efficiency of the algorithm. Data-Oriented Design (DOD) is a different way to approach program design that addresses these issues. Procedural programming focuses on procedure calls as its main elements, and OOD deals primarily with objects. DOD shifts the perspective of programming from objects to the data itself: the type of data, how it is laid out in memory, and how it will be read and processed during program execution. MAP takes advantage of both OOD and DOD in that base classes provide a clear modular structure that can be extended in the future and the data is structured such that the code accesses it in a less random manner, thus reducing cache misses.

As a first step toward verifying the new code, results were compared to those generated with DAC. Great care was taken to assure that the simulations being run by each code were as similar as possible. A wide variety of test cases have been used to compare the performance and results of the two codes including simple spheres, satellite configurations (i.e. the Mars Reconnaissance Orbiter, Cassini), re-entry geometries, and various other experimental setups (see Fig. 20 for an example of plume flow from a flat plate). In general for performance, MAP is anywhere from 42% faster to 6% slower than DAC, depending on the simulation. The resultant forces and moments are generally within ±2% of each other with heating within ±5%. MAP currently does not scale as well as DAC when parallel performance is considered, but this issue is a current subject of development. Please refer to Ref. 61 for a more complete comparison of the two codes.
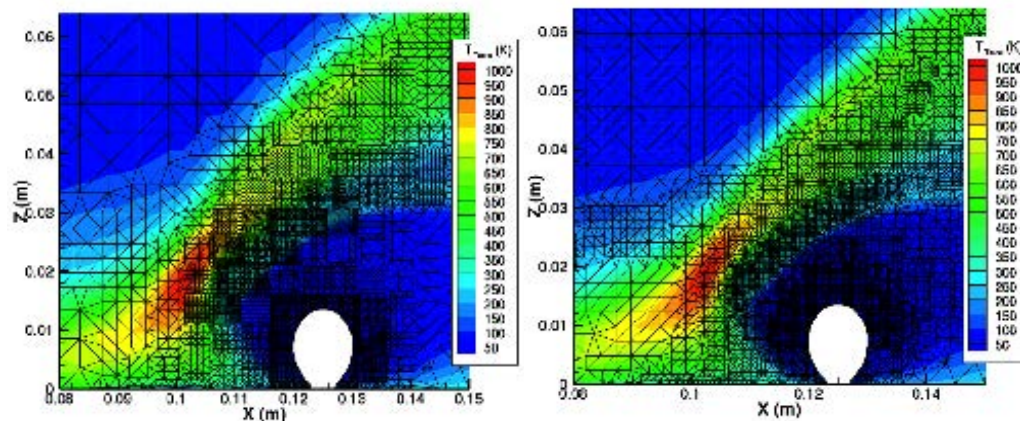

Figure 20. Adapted flowfield about a plume; a) DAC and b) MAP.[61]

There are also features in MAP that are currently unavailable in DAC. New physical models incorporated into MAP include an electronic energy level model (necessary for radiation calculations), an extended Quantum-Kinetic chemistry model,[62] and an updated electric field model. MAP also includes a three-level dynamic grid adaption scheme and a dynamic local timestepping scheme. See Ref. 60 for more information. Although in principle all of these models could be incorporated into DAC as well, the addition of these features in MAP was greatly facilitated by its OOD nature.

D. Shock Layer Radiation Database

The 4" diameter Electric Arc Shock Tube (EAST) facility[63] at NASA Ames is the Agency's only ground-test facility capable of producing flight like velocity, densities and compositions over conditions relevant for high-speed planetary entry where shock layer radiation would be expected to contribute significantly to aerothermal heating. ESM is using the EAST facility to build or significantly improve shock layer radiation databases for both high speed Earth and Venus, Mars or Titan entries. In addition, new EDL technologies such as inflatable or deployable entry systems are driving a need for measurements at lower pressures than those previously performed. To accomplish this task, the 24" diameter Low Density Shock Tube (LDST), also at NASA Ames, is being brought back online. The shocks produced in these facilities have similarity to the stagnation line in an entry scenario. Using spectroscopic techniques, an image is taken of the light emitted from the tube as the shock passes the test section. This image

provides spectrally and spatially resolved information on the radiation emitted from the hot region of gas behind a planar shock. The spectral resolution allows researchers to identify key radiating species (and with proper calibration, to determine their density), while the spatial resolution allows for determination of the time for the flow to evolve through the initial non-equilibrium region toward equilibrium. Integration over the spatial and spectral dimensions allows a measure of the total radiance emitted by the shock. Depending on the cameras, gratings and test section windows used, data can be obtained from the vacuum ultraviolet (VUV) through the infrared (IR) regions of the spectrum. While certain scales of entry are not matched in the shock tube (e.g. vehicle radius, duration of entry), the 1D profile obtained may be used to analyse reaction kinetic and radiation phenomena and serve as a benchmarking tool for predictive simulations. ESM funded work in these facilities has been published in Refs. 64-66.

The most recent tests in the EAST facility have focused on improving our understanding of shock layer radiation at conditions representative of Mars entry. At speeds relevant to most Mars entries, the primary radiant species are CO (mainly in the VUV), CN (in the visible), CO_2 (in the mid-wave IR), and some atoms such as carbon and oxygen. Prior work in the facility[67] produced a good baseline database for Mars and Venus, but these tests were run primarily in a fixed CO_2/N_2 mixture that was not equivalent to the Martian atmospheric composition, and thus the effects of freestream composition on relative radiative intensities were unknown. A series of tests was initiated in 2013 to obtain new radiation data for a range of compositions,[65] and the results were used to evaluate the sensitivities of key radiators to freestream composition. In general, radiance levels were only weakly affected by the amount of N_2 in the freestream, with the notable exception being CN. In addition, the values of certain key reaction rates were inferred by examining relaxation times as compared to theoretical estimates. Cruden et al. demonstrated that, for several key reactions, the rates inferred by this analysis differ significantly from those previously proposed by Johnston et al.[68] Quantum mechanical analysis of key reaction rates is currently underway within the Project, and these results will help to resolve these discrepancies and reduce the uncertainty in key reaction rates for Mars entry.

A second EAST entry was conducted at conditions selected to match the entry of MSL, which was equipped with sensors to determine the heat flux on the vehicle heatshield.[69] The peak heat fluxes and in-depth material response measured during flight by these instruments were fairly well predicted, however significant discrepancies were observed between measured and predicted heating rates after the peak heating point of the trajectory, with the predicted heat flux significantly lower than that measured. The discrepancy was largest near the stagnation line.[70] One hypothesis is that radiative heating in the mid-infrared from hot vibrationally excited CO_2 molecules could explain the discrepancy. Radiation from CO_2 was not considered during the design of the MSL heatshield, but was later determined to be a potentially significant contributor to the total entry heating for that mission. In addition, since the radiation was from the readily dissociated CO_2 molecule, it was expected to reach its maximum intensity at relatively low velocity, well after peak convective heating, when the shock wave was no longer strong enough to dissociate the CO_2 outright.

The MSL best estimated trajectory (BET) has been determined through analysis of the Mars Entry Atmospheric Data System (MEADS),[71] and is shown in Fig 21. Five points on the MSL trajectory were chosen for testing in the EAST facility. A gas mixture consisting of 95.8% CO_2, 2.7% N_2 and 1.5% Ar (by volume) is used to approximate the Martian atmosphere. Radiation from these shocks was measured from the VUV through Mid-Wave Infrared (MWIR). For this trajectory, the most important spectral ranges are identified as those corresponding to fundamental (4.3 μm) and overtone (2.7 μm) stretches of CO_2. Representative EAST Experiments are shown in Fig. 22. The figures show 3D measurements with wavelength on the x-axis and position on the y-axis. The shock is located at approximately 2 cm on the axis. Through most of the trajectory, features in the ultraviolet through visible are negligible and MWIR radiation is dominant. The summary of measurements at all five conditions is shown in Fig. 23. Here the cross-section of spectral radiance from 2-4 cm behind the shock front is averaged and presented for the UV-Visible and Mid-Infrared regions. At t = 96 s and beyond, the UV-visible signal is no longer distinguished from the noise level of the camera. In the mid-infrared, on the other hand, radiance is increasing through the trajectory until t = 85-96 s where the signal reaches its maximum level before decreasing at t = 104s. This increase is attributed to a rising CO_2 density as the shock density increases and its dissociation rate decreases. Near the end of the trajectory, the shock weakens enough that the lower post-shock temperature causes the radiance to begin decreasing again. The level of the MWIR radiance is orders of magnitude larger than in the visible range (note that a log scale is used in Fig. 23a). When the data from these shots are used to add a radiative heating estimate to the MSL entry environments, the resulting heat flux profile is in much better agreement with measured data. The results of this analysis are discussed in detail in a companion paper (Ref. 66).
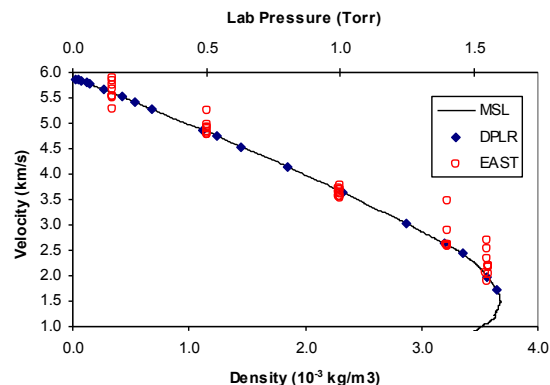
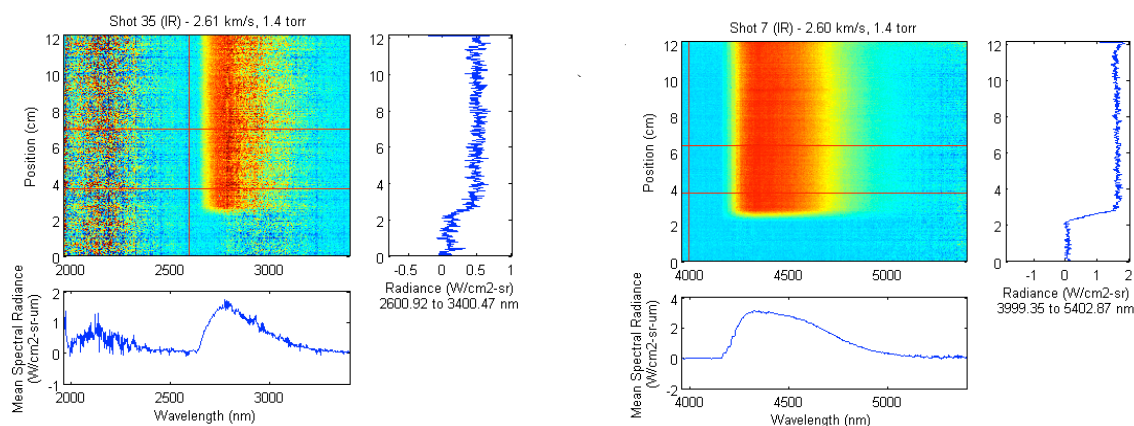**Figure 21. MSL Entry trajectory, with EAST test conditions overlayed.[66]**

Figure 22. Representative spectra from EAST testing; a) CO_2 overtone, and b) CO_2 fundamental.[66]
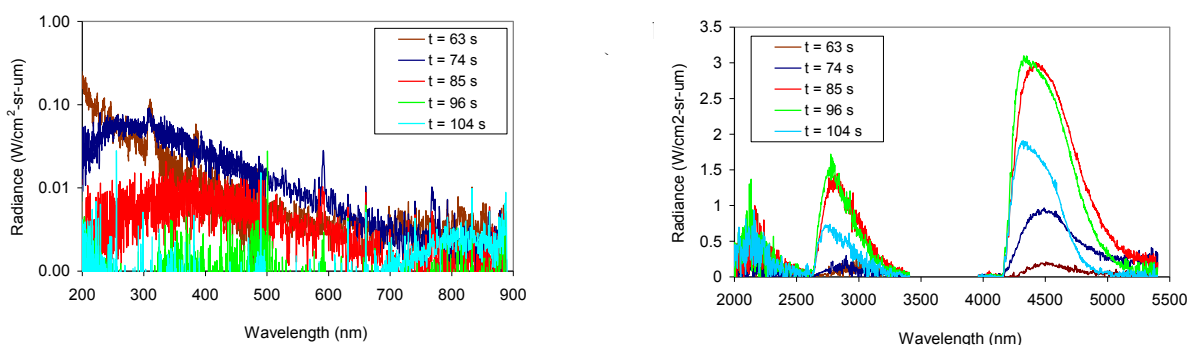

Figure 23. Radiance behind the shock at five trajectory points. (a) UV-NIR wavelengths, (b) MWIR wavelengths.[66]

E. HyperRad

The HyperRad radiation code was under development within the Hypersonics Project for several years, and one objective of ESM at its founding was to complete the code and make it available for mission use.[72-73] HyperRad is an extensible parallel code meant to compute fully coupled radiative heating of the gas and body surfaces in hypersonic flow and to provide spectra for comparison to experimental and flight data. The primary motivations behind the development of HyperRad are:

(1) extend and update the physical models utilized in NEQAIR and HARA;

(2) include atomic and molecular data from recent *ab initio* quantum chemistry calculations;

(3) provide fully 3D radiative transfer on structured and unstructured CFD grids.

An efficient and accurate line list-driven database has been implemented for both atoms and molecules of interest. For atoms, the list contains data merged from NIST, Vanderbilt and TOPBase atomic line datasets and currently includes lines of C, C^+, N, N^+, O, and O^+. For molecules, *ab initio* calculations (discussed in more detail in the following section) are used for electric dipole and quadrupole, magnetic dipole, and spin-forbidden transitions which include fine structure, pre-dissociation, and non-adiabatic corrections; currently included are lines of N_2, O_2, N_2^+, C_2, CO, CO^+, and CN. Line broadening and shifts due to the Stark effect are based on rate coefficients computed by a semi-classical method, and the resulting line-widths have been parameterized for efficiency with an analytical fit in temperature up to 50,000 K. Currently, HyperRad uses equilibrium excited-state population densities. For non-equilibrium conditions, physics-based modeling for excited-state populations are being implemented using coupled thermal, chemical, and radiative nonequilibria to provide significant physical fidelity compared to existing quasi-steady-state (QSS) models.[74]

Initial validation of the HyperRad code for equilibrium radiation simulations from the VUV to the IR was performed by Brandis et al.[73] by comparison with data from EAST and comparison to results from NEQAIR and HARA. Figure 24 shows the overall level of agreement between all three codes and EAST data.
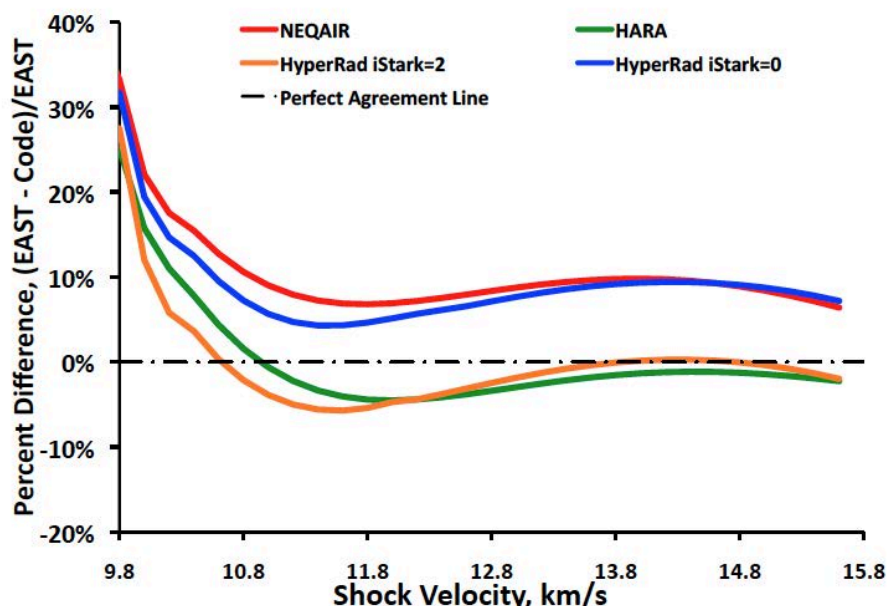

Figure 24. Overall percent disagreement of HyperRad, NEQAIR and HARA's prediction with respect to EAST from 170-1388 nm in air.[73]

Overall, agreement between the codes was quite good, with the primary differences between NEQAIR and HARA caused by differences in treatment of the Stark broadening parameter.[75] All three codes tend to underpredict radiation at low velocity, but in this case the total radiance is small, so the overall effect on vehicle design is negligible. Other discrepancies occur in the VUV and IR portions of the spectrum. More details on HyperRad and its initial validation can be found in Ref. 73. The final production version of HyperRad will include nonequilibrium radiation and full 3D radiative transport. A future paper is planned to show results from this code.

F. Spectroscopic Database

The accuracy of the radiation modeling codes is only as good as the database of frequencies and line intensities that are used for simulating the wavelength dependent radiative flux incident on a spacecraft or produced in ground tests. Historically, the NEQAIR spectroscopic database was based mainly on observed spectral transitions. However, with current computational power, quantum mechanical calculations can be used to generate accurate potential energy surfaces (PES) and intensity factors for spectroscopic transitions of all relevant diatomic molecules. One of

the great advantages of first principles calculations is that one is not restricted to states whose bands have been analyzed. As an example, in Fig. 25 we show the computed potential curves for CO, along with symbols designating the states that are included in Huber and Herzberg.[76] One can see that many more curves are computed than there are symbols. Furthermore, the calculations yield all couplings and transition moments between the various states. The symbols are placed at the experimentally determined equilibrium distance and experimentally determined vertical excitation energy. Another thing to note is in the high-energy regime, the potential curves show a great deal of structure that significantly departs from simple model potential energy curves, such as the Morse potential.
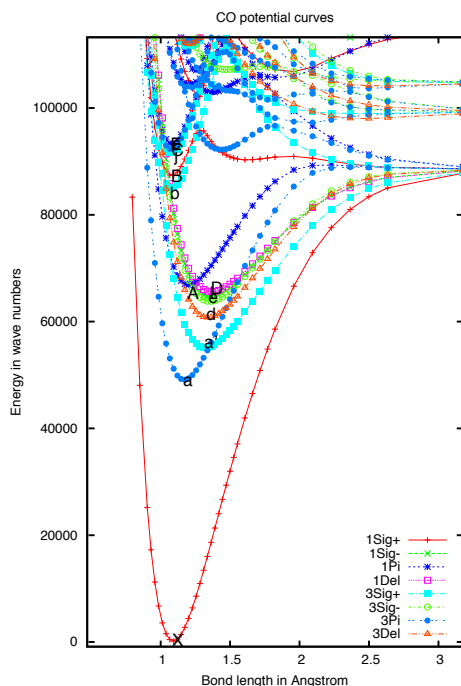

Figure 25. Calculated potential energy curves for CO for low-lying electronic states. The black letters denote the positions of the observed electronic states at the equilibrium bond length.

A primary objective was the prediction of molecular spectra up to the vacuum ultra violet for the species C_2, CN, CO, N_2, NO, O_2 and their cations. For the cations, this just involved valence excitations, while for the neutrals, low lying Rydberg states are also involved. The calculations are carried out in two steps: first we compute molecular orbitals (MOs), then we compute energies given the molecular orbitals using a modified version of the MOLPRO program. The calculations included many electronic states, and the average energy was minimized using the dynamic weighting scheme of Deskevich *et al.*[77] For neutrals, the low-lying Rydberg orbitals were determined after the valence orbitals. Once the electronic wave functions were determined, we computed transition matrix elements, spin-orbit matrix elements, and approximate overlaps between the wavefunctions at adjacent bond lengths. This methodology, though complicated, provides potential curves for valence and Rydberg states of comparable accuracy.

These data were used in the calculation of the ro-vibrational energy levels, using a code based on that reported in Ref. 78. This code allows coupling between different electronic states, and explicitly includes vibrational-rotational coupling with the proper rotational kinetic energy operator including fine structure effects. We computed all bound levels and all possible electric dipole, electric quadrupole, and magnetic dipole transition strengths. To facilitate the calculations, we first transformed the computed data to a diabatic basis. By this means, the derivative coupling matrix elements remain small at all bond lengths and can safely be neglected.

The same approach is used to compute the potential energy surface (PES) for triatomic molecules. In this case the PES is a function of three geometric variables (generally two bond lengths and one angle). As the energies are needed for many more molecular geometries than in the case of a diatomic molecule, the energy surface cannot be computed to the same accuracy. We are currently using this approach for C_3, C_2H and CO_2. As an example, the absorption spectrum for C_3 at 3000 K has been calculated for the wavelength range 140-200 nm. C_3 is a predominant

ablation product injected into the boundary layer from carbon phenolic based TPS, and is of interest to modeling of the radiative heat flux because it has a very strong X $^1\Sigma_g^+$-$^1\Sigma_u^+$ transition that might absorb some of the incident atomic radiation. The C_3 molecule has a linear ground electronic state, but the fundamental frequency of the bending mode is just 65 cm^{-1}, so this mode will be highly excited at typical boundary layer temperatures. Previous work[79] has characterized the electronic states of C_3 for energies up to 12 eV. Figure 26a shows a comparison of the calculated 4.3 K spectrum with the experimental spectrum of Monninger.[80] The computed spectrum for T = 3000 K is shown in Fig. 26b. Note that the peak intensity has shifted from 155-160 nm at 4.3 K to 172 nm at 3000 K and the detailed structure is no longer apparent at the higher temperature. However, that peak is favorably positioned for C_3 to absorb some of the incident N atom 174 nm radiation.
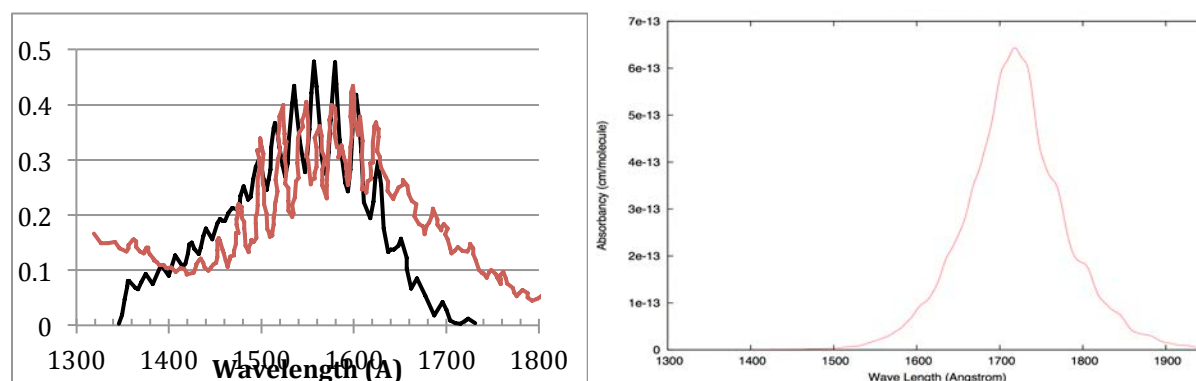

Figure 26. C_3 VUV absorption bands: a) 4.3 K in a solid Ne matrix. Black curve is the computed absorption spectrum and red curve is the experimental spectrum of Monninger et al. b) calculation at 3000K.
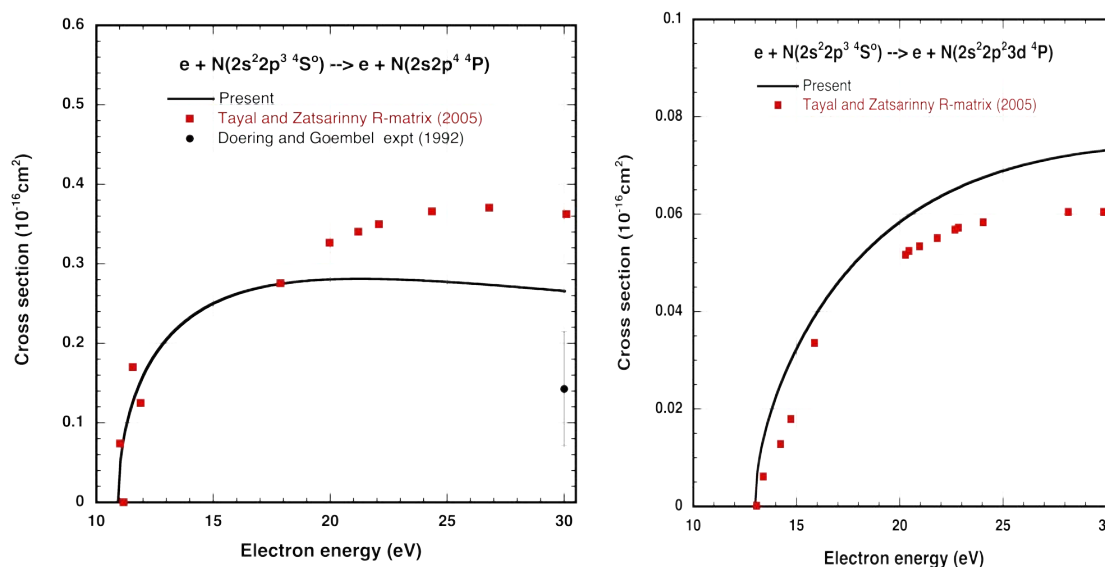

Figure 27. Electron impact cross section cross section of a) N $2s^2 2p^3$ ^4S_o – $2s2p^4$ ^4P and b) N $2s^2 2p^3$ ^4S_o – $2s^2 2p^2 3d$ ^4P (Ref. 82).

For the flight regime being considered, electron-atom/molecule collisions provide an efficient means of producing excited electronic states of the atoms and molecules in the flow field. These excited states are the predominant source of radiation observed during a hypersonic entry and play an important role in determining the internal energy and state distribution of the shock layer gases. Electron-atom/molecule collisions differ from heavy particle collisions in three aspects. First, the mass of an electron is more than four orders of magnitude smaller than the reduced mass of N_2 and its average speed (and hence its average collision frequency) is more than 100 times larger. Thus, even in the slightly ionized regime with ~1% electrons, the frequency of electron-atom/molecule

collisions is equal to or larger than that of heavy particle collisions. Second, the interaction potential between a charged particle (electron) and a neutral particle is longer range than neutral-neutral interactions. Hence electron-atom/molecule collision cross sections tend to be larger. Finally, a characteristic of electron-heavy particle collisions is that they generally produce a variety of excited state species whereas heavy particle collisions tend to produce a few specific excited states.

The present study covers the excitation/de-excitation of the full set of N, O and C states, including all transitions among 684 states of atomic nitrogen, 552 states of atomic oxygen and 915 states of atomic carbon. A perturbation method is used for computing cross sections for transitions between all of these atomic states as a function of electron energy. As examples of these calculations, Fig. 27 shows results for two transitions in atomic nitrogen. The single experimental data point at 30 eV in Fig 27a is by Doering and Goembel.[81] For atomic nitrogen, rate coefficients have been computed for 16,239 dipole-allowed transitions and 217,347 spin and symmetry forbidden transitions. See Ref. 82 for additional details of these calculations. Additional results to date of this work have been summarized in Refs. 83-84.

G. Shock Layer Radiation Model Validation

The shock layer radiation validation task is an omnibus activity, consisting of multiple components that are tightly coupled to the other radiation activities. Important results from this effort are published in Refs. 85-95. A few representative results are summarized in this section.

Radiative heating was identified as a major contributor to after-body heating for Earth entry capsules at velocities above 10 km/s. Because of rate-limited electron-ion recombination processes, many of the electronically excited N and O atoms produced in the high temperature/pressure fore-body remain as they expand into the after-body region, which results in significant after-body radiation. In addition, ablation products from a heatshield TPS were shown to increase the after-body radiation by nearly 40%, due primarily to the influence of CO on the vibrational-electronic temperature.[85] The commonly used one-dimensional tangent-slab radiation transport approach was shown to over-predict the radiative flux by as much as 50% in the after-body, therefore making the more computationally expensive ray-tracing approach (or a fully 3D radiative transport method) necessary for more accurate radiative flux predictions. Using this approach, comparisons with FIRE II measurements showed improved agreement with the addition of after-body radiation.[85]
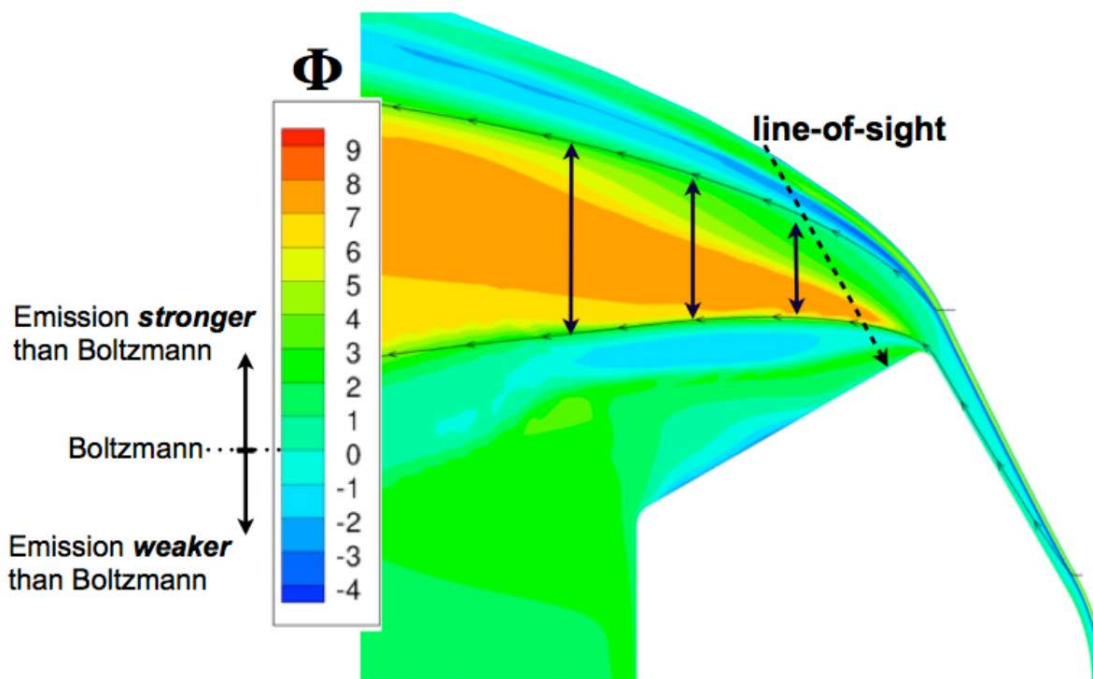

Figure 28. Values of Φ for Stardust at t = 46s (Ref. 85).

A parameter was defined in this study, Φ, to be the logarithm of the Saha-Boltzmann population divided by the Boltzmann population. Evaluating this parameter throughout an after-body flowfield for N allows the strongly radiating regions to be identified, an example of which is shown in Fig. 28. The observation that after-body radiation

is significant does not contradict the negligible Fire II and Apollo radiometer measurements for two reasons. First, these measurements did not capture the VUV region of the spectrum, which was shown in this study to contribute up to 7 times the non-VUV radiative flux. Second, these measurements had a lower sensitivity limit of roughly 2 W/cm^2, below which the radiometer read a value of zero. Therefore, a radiometer location that encountered just under 2 W/cm^2 of non-VUV radiative flux, and therefore produced a negligible radiometer reading, could have actually encountered up to 14 W/cm^2 of VUV and 16 W/cm^2 of total radiative flux. This value may be nearly equal to, if not greater than, the convective heating for most after-body flows, and therefore should be included in heating estimates. These comparisons provided confirmation that after-body radiation is a valid heating mechanism and one that requires consideration in future vehicle designs. This work has already led to mission requested analysis of backshell environments for the upcoming OSIRIS-Rex and InSight missions, and will likely impact all future blunt body entry missions for which radiation is a heating concern.

In another activity, new correlations for convective and radiative stagnation-point heating were provided for a variety of Earth entry conditions.[86] The correlations were based on the characterization of stagnation-point convective and radiative heat flux to an entry vehicle over a range of velocities, densities and nose radii. The simulations were compared with the established correlations of Fay-Riddell and Sutton-Graves for convective heating and Tauber-Sutton for radiative heating. Both the radiative and convective heating values were computed using state-of-the-art coupled LAURA/HARA simulations. The treatment of thermochemical nonequilibrium effects in the LAURA flowfield solution and non-Boltzmann modeling in the HARA radiation solution represented significant modeling improvements over the widely used previous Sutton-Graves convective heating correlation and the Sutton-Hartung radiative heating tables (which were used for the Tauber-Sutton correlations). The coupling of the radiation and flowfield not only affects the radiative heat flux to the vehicle's surface, but also the convective heat flux. Coupling removes energy from the flow, reducing enthalpy available to drive convective heating. At the same time, however, radiation absorbed in the boundary layer may increase heating by increasing the boundary layer temperature and energy.

A total of 648 LAURA/HARA solutions were used in the analysis in order to provide correlations that covered densities from $1x10^5$ to $5x10^3$ kg/m^3 and vehicle radii from 0.2 to 10m and velocities of 3 to 17 km/s for convective and 9.5 to 17 km/s for radiative heating. A comparison between the Tauber-Sutton correlation and Ref. 86, baselined to the main quantity of interest (total heat flux), is shown in Fig. 29. The updated fits show improved agreement with the LAURA/HARA solutions compared to previous correlations across the board (in terms of the mean, standard deviation and max error), especially when the Tauber-Sutton correlation is extrapolated, and provide a far wider range of parameters for which the fits are valid for Earth entry.
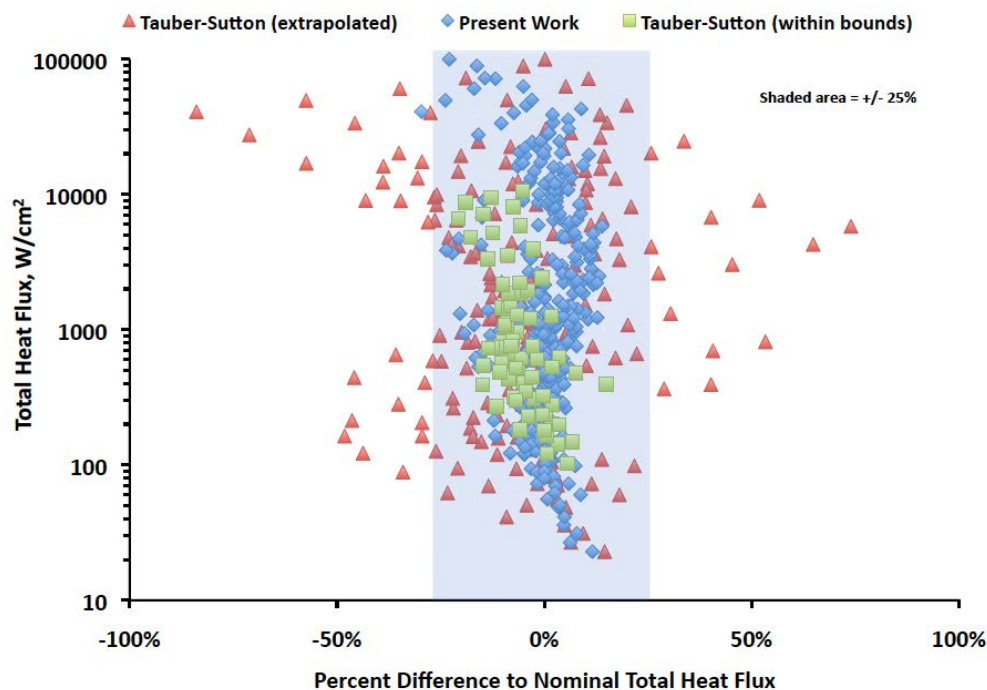

Figure 29. Comparison of current radiation heating correlation to previous works.[86]

H. High Enthalpy Aerothermal Database

As part of a three-year award funded by the NASA Space Technology Research Grants Program, ESM is collaborating with the Cal-Span University of Buffalo Research Center (CUBRC) to conduct a series of experiments simulating Martian atmospheric entry. The tests are being performed in the LENS-XX expansion tunnel facility. The LENS-XX facility is a unique national resource, and the only facility capable of reaching flight relevant enthalpies on real vehicle geometries in CO_2 for the purpose of constructing a ground based aerothermal database for future Mars entry missions. Previous attempts in shock tunnel facilities had mixed results,[96-98] presumably due to non-flight like excitation of CO_2 in the freestream. The following section gives a brief overview of testing to date; for more information see Refs. 99-100.

The tests are conducted on a 20.32 cm diameter sphere-cone with a 70° half-angle. This shape is geometrically identical to the MSL forebody heat shield outer-mold line (OML). The stainless-steel model is instrumented with thin-film heat flux, coaxial thermocouple heat flux, piezo-electric pressure, and forebody and aftbody radiometers for IR and VUV shock layer emission. The instruments are concentrated along the centerline of the model from windside to leeside along the forward facing heat shield with additional off-centerline instruments. Instrumentation is included at the locations of the 7 thermocouple plugs that were installed in the MSL heatshield. The model with instruments installed is shown in Fig. 30a. The installed model in the facility at nominally 16° angle-of-attack is shown in Fig. 30b.

The LENS-XX expansion tunnel was used to study surface distributions for freestream velocities ranging from 1.7 to 11.6 km/s, spanning the potential range of entry velocities for Mars, including potential high velocity entries for future missions. The test gas is 100% CO_2, which the expansion tunnel accelerates by directly increasing kinetic energy and maintaining a fairly low level of thermal excitation in the freestream test gas. A sample Schlieren image obtained during a run at approximately 6 km/s is compared with CFD prediction in Fig. 30c showing good agreement with shape and stand-off distance.
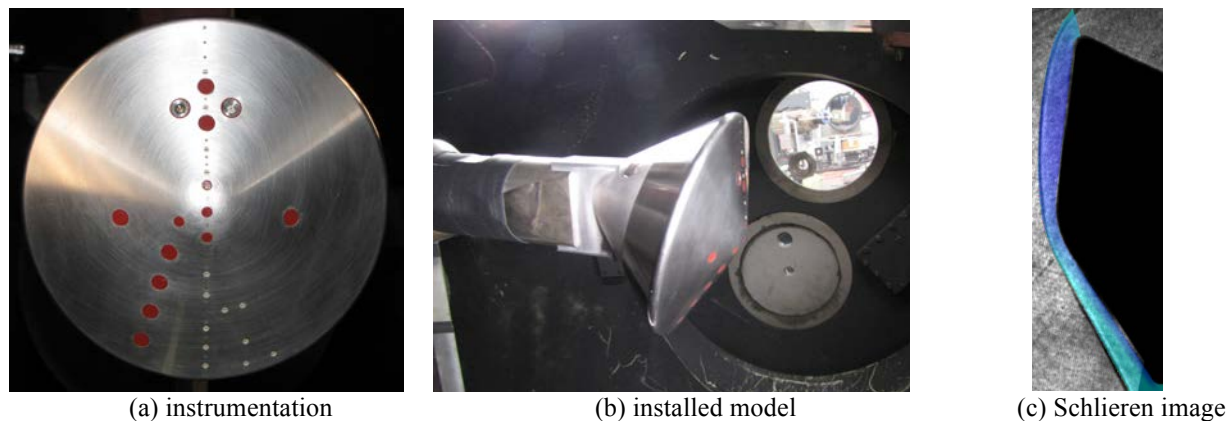

(a) instrumentation   (b) installed model   (c) Schlieren image

Figure 30. LENS-XX a) model instrumentation, b) installation, and c) shock shape.

Typical heat flux distributions along the centerline are shown in Fig. 31. The stagnation point of the heat shield is on the left of each graph roughly at -5 cm. The leeward side of the heat shield is to the right side of each graphic. Reference CFD solutions are plotted assuming two different surface catalycity models: completely non-catalytic and super-catalytic (corresponding to 100% CO_2 surface mass fraction). These extremes act as rough bounds on the expected total convective heat flux. At higher enthalpy and lower density, the range of heat flux between the limits increases substantially. At high enthalpy and low Reynolds number like in Fig. 31a, measured laminar heating has been observed to consistently be at or just above the non-catalytic prediction from a number of run conditions. At higher densities, such as Fig. 31b, the CFD solutions collapse and become indistinguishable from the laminar data. For some high Reynolds numbers, transition onset has been observed to occur as in Fig. 31c. The transition onset correlates well to a Re_θ=200 criterion, which is consistent with observations on various blunt bodies in a number of other facilities. However, an interesting related observation is that several runs do not show an end to the transition process as might be expected as Reynolds number continues to increase further.
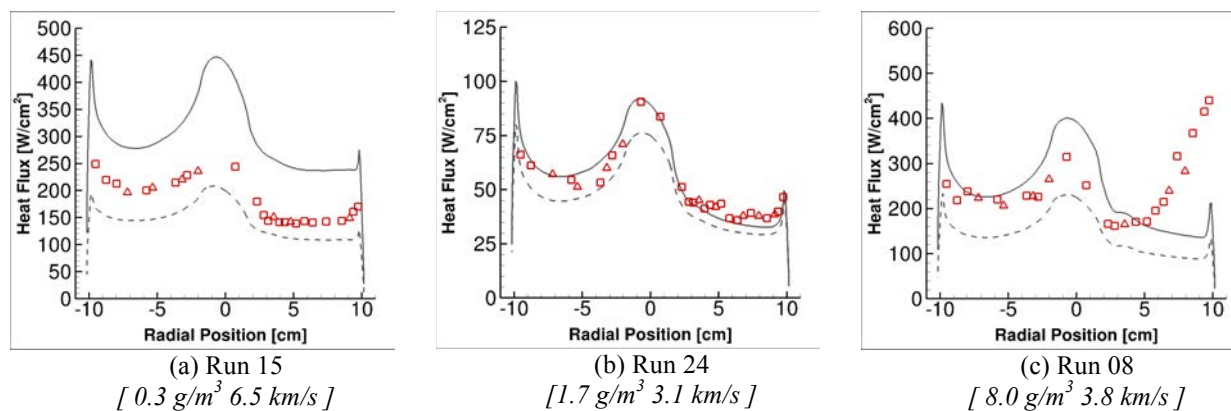
(a) Run 15
[0.3 g/m³ 6.5 km/s]

(b) Run 24
[1.7 g/m³ 3.1 km/s]

(c) Run 08
[8.0 g/m³ 3.8 km/s]

Figure 31. Laminar and turbulent surface heat flux along center plane at various conditions.[100]

The measurement of radiation produced behind the model shock layer is a secondary objective of the experiments through the use of a number of radiometers located on the forebody heat shield and aftbody of the model. An example is shown in Fig. 32a, which plots the transient response of a radiometer on the forebody (R2) and the aftbody (R3). Interestingly, R2 shows a non-zero signal first, rising at about 14.7 ms. This early detection is presumed to be caused by radiative emission from the traveling shock approaching the front of the model as the facility starts. Radiometer R3 shows no such sensitivity. At steady state, from approximately 16.3 to 16.8 ms, the forebody and aftbody radiation is observed to be virtually the same (Fig. 32b), despite the large difference in density between the stagnation and aftbody regions. It was also observed that this trend holds and scales linearly with freestream density (roughly corresponding to number of emitting molecules). Since the bulk of the observed radiation in this relatively low speed test is likely due to CO_2, this result is very interesting and highlights the potential importance of CO_2 MWIR radiation not only to the forebody, but also the afterbody of future Mars missions.

(a) transient response at 8 g/m³
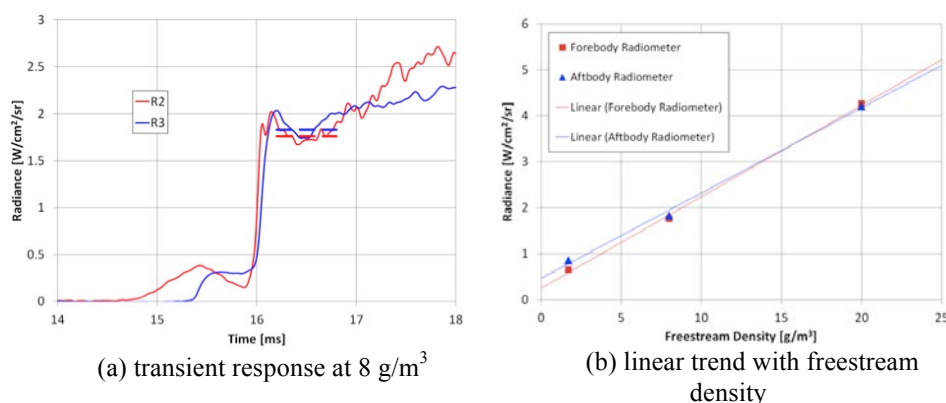
(b) linear trend with freestream density

Figure 32. Integrated IR radiance measurements of forebody and aftbody at 3 km/s (Ref. 100).

The data returned so far from LENS-XX are encouraging, but open questions remain about freestream quality, and some of the results obtained do not agree well with theoretical predictions. Testing at high enthalpy in CO_2 is fundamentally difficult because the molecule is readily excitable with relatively low energy input. As a way to better understand the flow physics, a collaborative effort has been initiated to obtain high-enthalpy heat-transfer, surface pressure and shock-visualization data in the Caltech Hypervelocity Expansion Tube (HET). In previous studies,[101-103] conducted while HET (Fig. 33) was located at the University of Illinois Urbana-Champaign, the performance of the facility at a 3 km/s condition was demonstrated with heat-transfer measurements (Fig. 34) on a 70-deg sphere-cone geometry. Additional testing will be conducted in 2015 to obtain data in the 2 km/s to 4 km/s range on the same model with additional instrumentation.
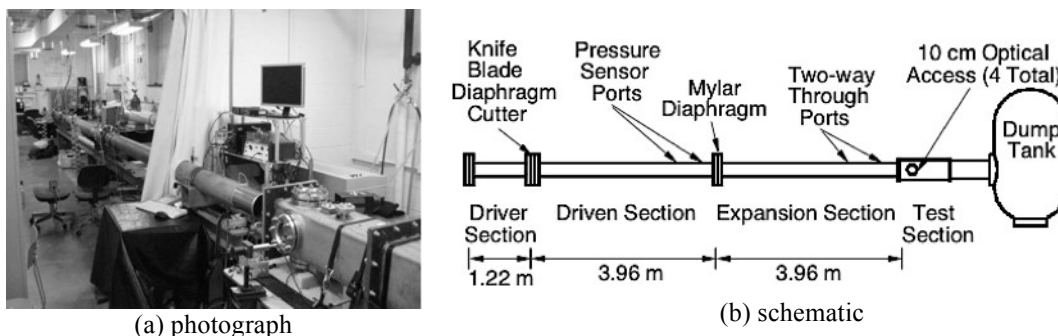
(a) photograph   (b) schematic
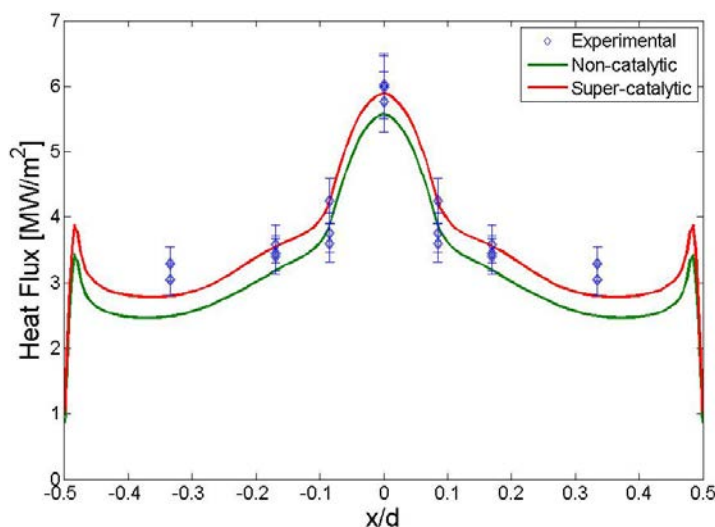
Figure 33. Caltech HET Facility

Figure 34. Heat-transfer measurement and comparison with US3D predictions.[101]

I. Roughness Testing – Ballistic Range

Surface roughness can induce boundary-layer transition to turbulence during entry, bypassing natural smooth-wall transition mechanisms. This effect is important for planetary entry because most entry heatshields are protected by ablative TPS material, which will develop a natural roughness pattern as it ablates. Turbulent flow results in more severe convective heat transfer rates and skin friction, which can impact the design requirements of the heatshield of an entry vehicle. Surface roughness can further augment turbulent convective heat transfer and skin friction, above smooth-wall values, through interactions with the wall-bounded shear layer over the entry vehicle.[104]

For example, analysis of data returned from the instrumented heatshield of the MSL entry vehicle[0] indicated that the rapid progression of the transition front from the leeward shoulder to the nose cap was consistent with transition induced by surface roughness.[9] It is clear that roughness effects will impact TPS sizing and margins for the severe entry environments encountered at the giant planets or at Venus, as well as for future Mars missions. Therefore, it is important to develop a better understanding of both the expected heating augmentation and the acceleration of transition to turbulence due to surface roughness. One approach to better understand the effects of roughness on both transition and turbulent aeroheating is through testing in a free-flight (ballistic range) facility. This section discusses a series of tests initiated under the Hypersonics Project and completed within ESM. The results summarized herein can be found in Refs. 105-107.

Due to the complex nature of the interactions between surface roughness and the boundary layer, the effects of surface roughness on transition and heat-transfer augmentation have typically been accounted for through various semi-empirical correlations developed from data obtained in ground and flight tests conducted in air. Prior tests in the free-flight ballistic range found that isolated roughness elements on blunt bodies were more effective, in terms of the roughness Reynolds number, at tripping the flow to turbulence in CO_2 than when air was the test gas.[108] This result raised the question of whether the established correlations for the effects of distributed roughness were applicable in the CO_2-dominated atmospheres of Mars and Venus.

In order to help answer these questions, experiments were performed in the Hypervelocity Free Flight Aerodynamic Facility (HFFAF) ballistic range at NASA Ames Research Center.[109] The tests were conducted in both CO_2 and air to provide a direct comparison with established correlations. The facility employs a two-stage light gas gun to launch model entry vehicles through an enclosed test section filled with a quiescent test gas at ambient room temperature. The test-section pressure and gas composition are controllable to allow simulation of flight through different planetary atmospheres, and to allow independent variation of Mach and Reynolds numbers. Turbulent transition was determined during flight using IR imagery of the model face; a sudden increase in surface temperature, outside of that predicted by laminar flow theory, was interpreted as transition. Aeroheating was measured by taking successive images of the model; the temperature rise between the first and second images could then be converted to an estimated heat transfer rate during that portion of flight.

The augmentation of turbulent convective heat transfer due to distributed (sand grain) roughness was measured on the conic frusta of 30° and 45° sphere-cones in flight at speeds between 2.8 and 3.6 km/s. Freestream Mach numbers ranged from 8 to 10, and freestream Reynolds numbers, based on the nose radius of 7.62 mm, ranged from 0.13×10^6 to 0.5×10^6. Figure 35 shows an example of some of the processed data from these tests, showing deduced heat transfer on the model surface. The results obtained in both air and CO_2, (Ref. 106), were in good agreement with the correlation of the Passive Nosetip Technology (PANT) Program,[110] as shown in Fig. 36. Turbulent heat transfer augmentation factors as high as 1.8 were found to correlate well with the smooth-wall roughness Reynolds number, Re_k, for both test gases.
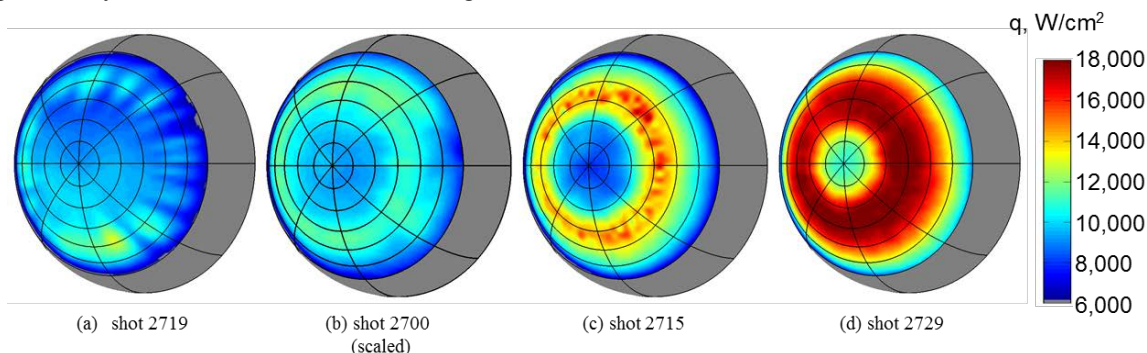

(a) shot 2719   (b) shot 2700 (scaled)   (c) shot 2715   (d) shot 2729

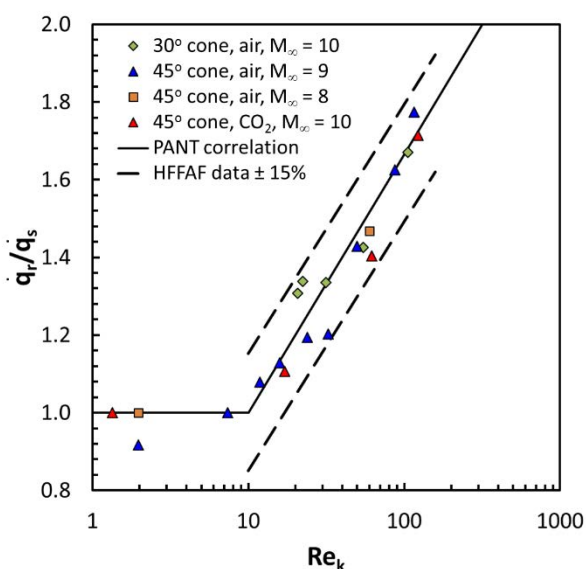**Figure 35. Heat-flux distributions determined for representative tests in CO_2 (Ref. 106).**

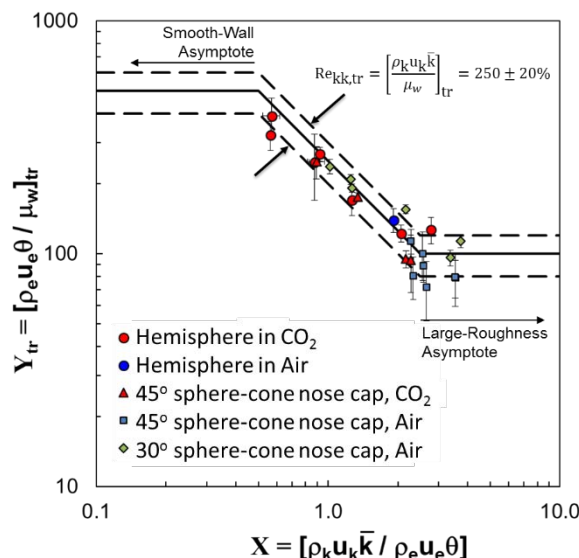**Figure 36. Rough-to-smooth wall heat-transfer ratio vs. turbulent roughness Reynolds number.[107]**

Figure 37. Transition correlation for blunt bodies with distributed roughness in hypersonic free flight in CO_2 and in air.[107]

Distributed surface roughness was employed on the sphere-segment nose caps for the tests reported in Ref. 106 in order to ensure a fully-developed turbulent boundary layer on the cone segments. As a consequence these tests also yielded roughness-induced transition data in both test gases. Further transition tests were conducted on hemispherically shaped models at flight speeds of 5 km/s (freestream Mach number of 20 in CO_2, and freestream Reynolds number of 0.9 x 10^6, based on the nose radius of 14.29 mm), and the results were reported in Ref. 107. Sample results are shown in Fig. 37, which plots a transition Reynolds number, Y_{tr}, as a function of a disturbance parameter, X, at onset of transition. Transition onset correlated well with a constant laminar roughness Reynolds number ($Re_{kk, tr}$) and was in agreement, within the bounds of experimental uncertainty, with the critical value of 250 ± 20% established in Ref. 111 for transition in air.

J. Roughness Testing – Langley Mach 6

An additional investigation into the effects of distributed roughness on boundary-layer transition and turbulent heating augmentation for blunt-body reentry vehicles was conducted in the NASA LaRC 20-Inch Mach 6 Air Tunnel. The data from this tunnel are highly complimentary to those from the Ames HFFAF because the test technique permits rapid model fabrication and global heat-transfer data to be obtained through phosphor thermography. In addition, the relatively rapid throughput of the facility permits a large number of tests to be run in a short time, which enables exploration of a large parameter space. The ESM project conducted testing over a range of free stream Reynolds numbers sufficient to produce laminar, transitional and fully turbulent flow. The test articles were hemisphere and sphere-cone geometries. A complimentary CFD study was conducted to provide boundary-layer parameters for correlation of the transition data and turbulent heating predictions for comparison to the measured, roughness-augmented turbulent heating distributions. Preliminary results from this research have been presented in Ref. 112.
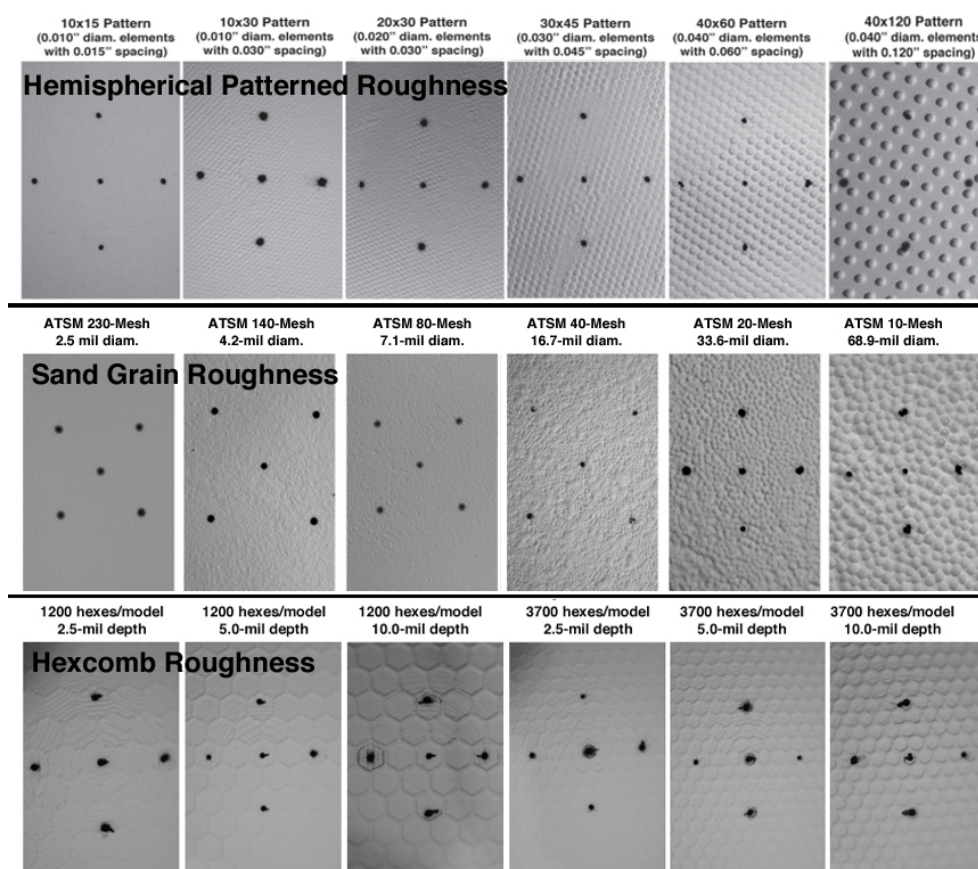

Figure 38. Model roughness types and scales, each image ~1-in. height.[112]

Three different forms of distributed roughness were considered in this work: pattern roughness comprised of arrays of hemispherical protrusions, sand-grain roughness formed by random distributions of controlled size particles, and recessed hexcomb roughness (roughly analogous to that expected as a result of ablation of a reinforced

material such as SLA-561V or Avcoat). Sample images of the range of roughness scales for each type are shown in Fig. 38. All roughness models were constructed through a ceramic casting process, but the process for fabricating the molds for casting the models differed depending on the roughness type. The hemispherical pattern roughness was created through chemical etching of metallic shells, from which molds were then created. The distributed sand-grain roughness models were formed by coating a smooth plastic pattern with adhesive, immersing it into a bed of glass beads of specified diameter, and finally making a mold from this article. The hexcomb roughness patterns were specified in a CAD package and then plastic resin patterns were formed through stereo-lithography, from which molds were created.

All forms of distributed roughness were highly effective in promoting earlier transition and producing higher turbulent heating levels than for a smooth model. Sample global heating images for each roughness type are shown in Fig. 39. Depending on roughness height scale and test Reynolds numbers, turbulent heating levels up to almost 100% higher than smooth-wall turbulent levels were measured. These data, together with the data taken in the Ames ballistic range, will be used to develop new roughness heating augmentation models in support of future planetary entry mission designs.
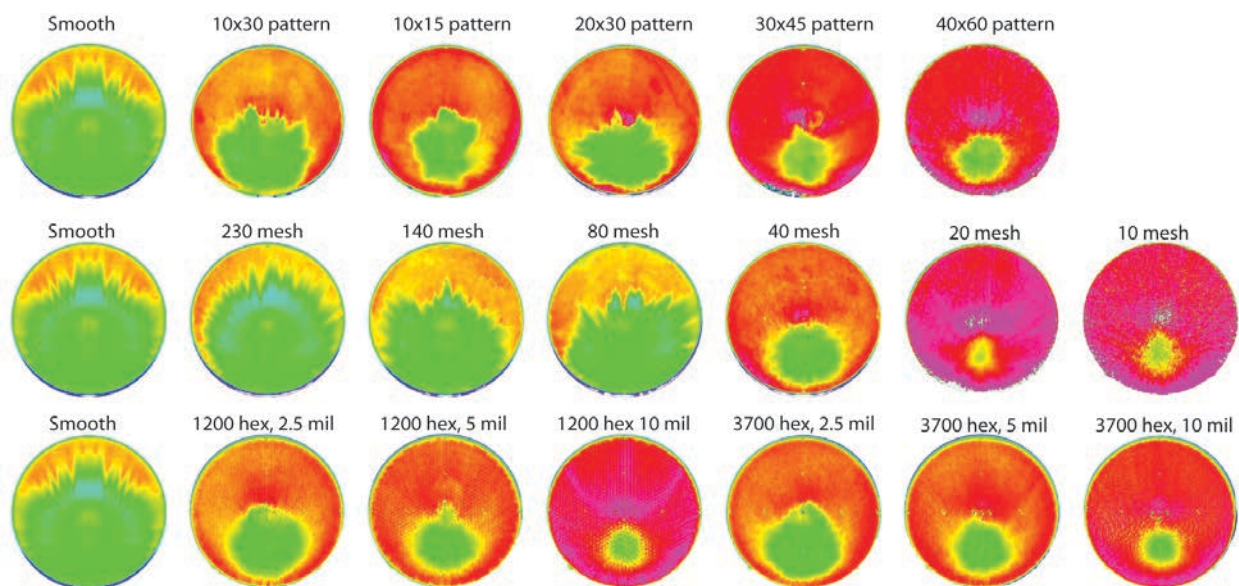

Figure 49. Model roughness effects on heating, $Re_\infty = 6.6 \times 10^6$/ft, α = 16-deg (Ref. 112).

K. SWTBLI Uncertainty

The NASA Hypersonics Uncertainty working group, begun under the Hypersonics Project in 2010, explored several sample problems with a goal of quantifying the uncertainty in the current state of the art simulation tools for the prediction of mission relevant aerothermodynamic phenomena.[113] One of these groups, the Shock Wave Turbulent Boundary Layer Interaction (SWTBLI) working group,[114] continued its efforts under the ESM Project. As part of this work, an extensive database of hypersonic 2D SWTBLI experiments (both compression corner and impinging shock) was documented, and their value for CFD calibration was assessed. During collection, emphasis was placed on datasets with pressure and heating data throughout the interaction regime, although some datasets with shear stress and flowfield profiles were also included. For those cases deemed suitable for use in CFD calibration, computed results were presented using several current production NASA CFD solvers and methods. The results and findings were published in a pair of NASA Technical Memoranda[115-116] along with accompanying data DVD's. Table 1, from Ref. 115, summarizes the relevant experimental data. Reference numbers in the Table refer to Ref. 115.
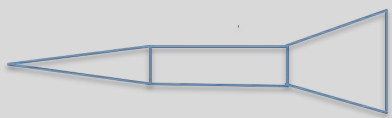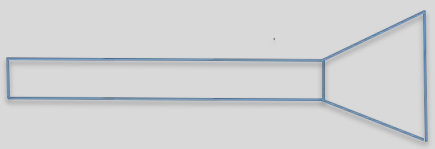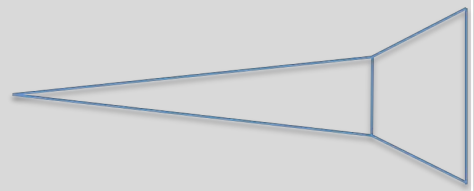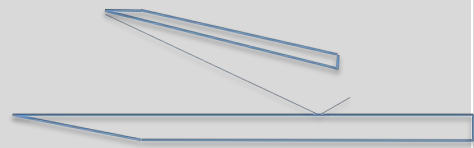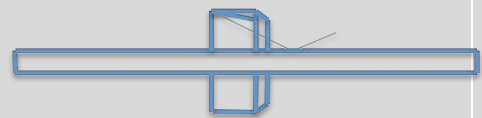
Hypersonic Experiments	References	Mach Number	Data Type
2D-Compression Corner	Coleman & Elfstrom (13,14 &15)	9	p_w, q_w
	Holden(12)	8.2,11.3	p_w, q_w,, c_f Schlieren, Limited surveys
Cone-Cylinder-Flare	Kussoy & Horstman(16)	7.2	p_w, q_w limited surveys
	Holden(12)	7.19	p_w, q_w, c_f
Hollow-Cylinder-Flare	Williams(9) Murray et al.(8)	8.9	p_w, q_w,
Axisymmetric Cone-Flare	Holden(12,17,18 &19)	11,13	p_w, q_w Schlieren, limited surveys
2-D Incident Shock Wave	Kussoy & Horstman(20)	8.2	p_w, q_w,
	Holden(12)	8, 11	p_w,q_w, Schlieren
	Schülein(7)	5	p_w, q_w, c_f Surveys, Shadowgraph
Axisymmetric Impinging Shock on Hollow Center Body	Murray(8 & 10), Mallinson(11)	8.9	p_w, q_w, Schlieren

Table 1. Two-Dimensional and Axisymmetric Hypersonic SWBLI Experiments.[115]

Results from the CFD comparisons showed that agreement between the two-equation turbulence models (such as the Shear Stress Transport model – SST) and experiment was generally good, but the SST model in particular tended to overpredict the extent of separation for compression corner SWTBLI and underpredict for impinging shock SWTBLI. SST also tended to overpredict heat transfer in the post-reattachment region.[116] Results from this work will be used to guide turbulence model improvements in the future.

L. M-SAPE Development

The Multi-mission System Analysis for Planetary Entry (M-SAPE) was originally developed within the In-Space Propulsion (ISP) program in the Science Mission directorate (SMD) as a tool to enable rapid trades for Mars Sample Return (MSR) Earth entry vehicle concepts.[117] As ISP budgets began to shrink, ESM agreed to partner with them to expand the capabilities of the tool for other missions as well, with the goal of creating a general systems analysis capability that could be used during the proposal phase of new entry missions to enable rapid turnaround mission design with increased engineering fidelity in the early phases of the design process.

M-SAPE, in its current form, is capable of performing system analysis for an Earth entry vehicle suitable for sample return missions. The system includes geometry, mass sizing, impact analysis, structural analysis, flight mechanics, TPS sizing and margin assessment, and a web portal for user access. Reference 118 provides details of the M-SAPE architecture, modules, and sample results.

The current M-SAPE vehicle design concept is based on Mars sample return (MSR) Earth entry vehicle design, which is driven by minimizing risk associated with sample containment (no parachute and passive aerodynamic stability). Two generalized configurations are modeled in M-SAPE. The first is the "MSR" configuration, in which the payload is encapsulated within a foam-filled impact sphere. The second is a "Non-MSR" configuration, in which the payload is nested in impact foam, with no surrounding impact sphere.

By exploiting a common design concept, any sample return mission will benefit from significant risk and development cost reductions. The design provides a platform by which technologies and design elements can be evaluated rapidly prior to any costly investment commitment.

An important goal for M-SAPE is to provide an integrated environment such that a low fidelity system analysis and trade can be performed in hours (not weeks or months) with sufficient hooks to perform high-fidelity analysis in days. The system is designed to help analysts to gain a better understanding of various entry system concepts and their limitations. The role of discipline experts in the systems analysis process is indispensable and cannot be replaced by any tool. However, M-SAPE helps to improve the performance of the systems analysis team by automating and streamlining the process, and this improvement can reduce the errors resulting from manual data transfer among discipline experts. The process improves and accelerates design activities such as trade studies, sensitivity analyses, Monte Carlo analyses, and vehicle optimization.
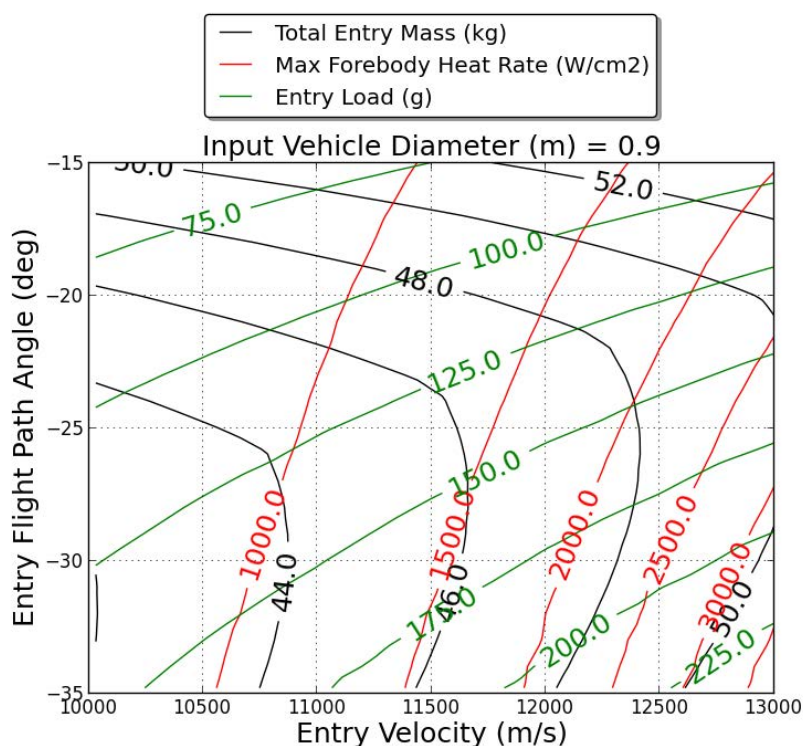

Figure 40. Sample M-SAPE Trade Space for MSR Model.[118]

Another goal of M-SAPE is to use existing software components, especially open-source software, to avoid unnecessary software development and licensing issues. M-SAPE is a loosely coupled system that uses Python

language (platform-independent open-source software) for integration. Development has relied heavily on the object-oriented programming capabilities available in Python. Modules are provided to interface with commercial and government off-the shelf software components.

Figure 40 shows the sample results for various entry velocities and flight path angles. The vehicle mass ranges from 34-62 kg. The entry load is a strong function of flight path angles and can vary from 75 to 230 Earth g's. The maximum heat rate is primarily a function of the entry velocity, and it varies between 1000-3000 W/cm^2.

At the current time the future of M-SAPE is somewhat uncertain as ISP has ended, along with the SMD contribution to finishing the code. The ESM project is working with the Human Architecture Team (HAT) to modify M-SAPE for use in their architecture studies, with the intent to deliver a product by the end of 2015.

V. Conclusions

The NASA Entry Systems Modeling Project is currently entering its third year of execution. In its first two-plus years, the project has generated XX conference papers and journal articles, and many more oral presentations. The work conducted by the project is generally in the TRL 2-6 range for both software and hardware deliverables, and is focused primarily in two technical areas: Aerosciences and Materials. In the Aerosciences technical area, the Project has already delivered two new aerothermal CFD codes to NASA – US3D and FUN3D – that are slated to succeed the current state of the art of DPLR and LAURA. If this transition is successful, it is likely that the US3D and FUN3D codes will be the most infused technologies in the entire Game Changing Development Program. In addition, the team is developing new DSMC capability, a vastly improved capability to accurately simulate shock layer radiation and validate those simulations, roughness induced heating augmentation databases, and a first of its kind high enthalpy aerothermal database in CO_2. These capabilities are already having impact on the design and development of current NASA missions, including Orion/MPCV, OSIRIS-Rex, and InSight. In the materials area. the team is developing flexible TPS technology that will enable the use of HIADs for exploration class missions to Mars, advanced ablator technology using novel conformal felts and new resins, and a radical improvement to the current state of the art in ablative response modeling, ranging from a suite of new ground validation data to a high fidelity response model, tight coupling of CFD and ablative material response, and an engineering fidelity design tool that will change the way that TPS systems are designed and sized.

Additionally, the ESM Project continues to adapt to the needs of the NASA EDL community, tackling the most important challenges in the discipline and showing that changes can be made on a three-year design cycle. In 2015, a new Project element has begun that will demonstrate controlled propellentless deorbit from Low Earth Orbit. More new starts are planned for 2016 that will change the way that entry systems are designed and built.

Acknowledgments

References

[1]Braun, R.D. ad Manning, R.M., "Mars Exploration Entry, Descent and Landing Challenges," *Journal of Spacecraft and Rockets*, Vol. 44, No. 2, 2007.

[2]Drake, B., "Human Exploration of Mars Design Reference Architecture 5.0" NASA SP-2009-566, July 2009.

[3]Cianciolo, A.M. et al. "Entry Descent and Landing System Analysis Study: Phase 1 Report," NASA TM-2010-21620, July 2010.

[4]Steltzner, A., "Mars Science Laboratory Entry, Descent and Landing System," IEEE Paper No. 2006-1497, Mar. 2006.

[5]Anon, "NASA Strategic Plan 2014," NASA Document NP-2014-01-964-HQ, 2014.

[6]http://www.nasa.gov/offices/oct/strategic_integration/grand_challenges_detail.html. Accessed Nov. 19, 2014.

[7]Adler M., Wright, M., Campbell, C., Clark, I., Engelund, W., and Rivellini, T., Entry, Descent and Landing Roadmap: Technology Area 09, NASA, 2012.

[8]Moyer, C.B. and Rindal, R.A., "An Analysis of the Coupled Chemically Reacting Boundary Layer and Charring Ablator, Part II: Finite Difference Solution for the In-Depth Response of Charring Materials Considering Surface Chemical and Energy Balances," Technical Report 66-7 Part II, Aerotherm, March 1967.

[9]White, T., Mahzari, M., Bose, D., and Santos, J., "Post-flight Analysis of the Mars Science Laboratory Entry Aerothermal Environment and Thermal Protection System Response," AIAA Paper No. 2013-2779, June 2013.

[10]Lachaud, J. and Mansour, N., "Porous Material Analysis Toolbox Based on OpenFOAM and Applications," *Journal of Thermophysics and Heat Transfer*, Vol. 28, No. 2, pp. 191-202, 2014.

[11]Lachaud, J., van Eekelen, T., Scoggins, J., Magin, T., and Mansour, N., "Coupled Chemical Equilibrium Ablation Model and Analysis of Boundary Layer and Pyrolysis Gas Flows Within a Porous Iso-Flux Sample," AIAA Paper No. 2015-xxxx, Jan 2015.

[12]Mansour, N., Panerai, F., Martin, A., Parkinson, D., MacDowell, A., Haboub, A., Sandstrom, T., Fast, T., Vignoles, G., and Lachaud, J., "A New Approach to Light Weight Ablators Analysis: From Micro-Tomography Measurements to Statistical Analysis and Modeling," AIAA Paper No. 2013-2768, June 2013.

[13]Panerai, F., Martin, A., Mansour, N., Sepka, S., and Lachaud, J., "Flow-Tube Oxidation Experiments on the Carbon Preform of PICA," *Journal of Thermophysics and Heat Transfer*, Vol. 28, No. 2, pp. 181-190, 2014.

[14]Wong, H., Peck, J., Edwards, R., Reinisch, G., Lachaud, J., and Mansour, N., "Measurement of Pyrolysis Products from Phenolic Polymer Thermal Decomposition," AIAA Paper No. 2014-1388, Jan. 2014.

[15]Panerai, F., Mansour, N., Lachaud, J., and Martin, A., "Experimental and Numerical Study of Carbon Fiber Oxidation," AIAA Paper No. 2014-1208, Jan. 2014.

[16]F. Panerai, "Microscale Modeling and Characterization of Carbon-Based Ablators Decomposition," in: M. Panesi, O. Chazot (Eds.), NATO-STO-VKI Lecture Series, *Radiation and gas-surface interaction phenomena in high-speed reentry*, von Karman Institute for Fluid Dynamics, 2014, Paper No. 8.

[17]H.-W. Wong, J. Peck, R. Edwards, G. Reinisch, F. Panerai, J. Lachaud, N.N. Mansour, "Quantitative Determination of Species Production from the Pyrolysis of a Phenol-Formaldehyde Resin," *Polymer Degradation and Stability*, (submitted, 2014).

[18]Wong, H. and Lachaud, J., "Quantitative determination of species production from the pyrolysis of the Phenolic Impregnated Carbon Ablator (PICA)," AIAA Paper No. 2015-xxxx, Jan 2015.

[19]J. Lachaud, Y. Aspa, G.L. Vignoles, "Analytical Modeling of the Steady State Ablation of a 3D C/C Composite," *International Journal of Heat and Mass Transfer*, 51 (2008) 2614-2627.

[20]Wright, M. J., White, T. R., and Mangini, N., "Data Parallel Line Relaxation (DPLR) Code User Manual: Acadia -Version 4.01.1," NASA TM 2009-215388, 2009.

[21]Empey, D., Gorbunov, S., Skokova, K., Agarwal, P., Swanson, G., Prabhu. D., Mangini, N., Peterson, K., Winter, M., and Venkatapathy, E., "Small Probe Reentry Investigation for TPS Engineering (SPRITE)," AIAA Paper No. 2012-0215, 2012.

[22]Muppidi, S., Barnhardt, M., Palmer, G., Mansour, N., Wright, M., and Lachaud, J., "Toward Ablative Material Response Coupling in DPLR," AIAA Paper No. 2014-2120, June 2014.

[23]Kirk, B, Peterson, J., Stogner, R., and Carey, G., "libMesh: A C++ Library for Parallel Adaptive Mesh Refinement/Coarsening Simulations," *Engineering with Computers*, 22(3-4), pp. 237-254, 2006.

[24]Amar, A.J., Calvert, N.D., and Kirk, B.S., "Development and Verification of the Charring Ablating Thermal Protection Implicit System Solver," AIAA Paper No 2011-0144, Jan. 2011.

[25]Chen, Y-K, and Milos, F.S., "Two-Dimensional Implicit Thermal Response and Ablation Program for Charring Materials," *Journal of Spacecraft and Rockets*, Vol. 38, No. 4, 2001, pp. 473-481.

[26]Kirk, B., Stogner, R., Bauman, P., and Oliver, T., "Modeling Hypersonic Entry with the Fully-Implicit Navier-Stokes (FIN-S) Stabilized Finite-Element Flow Solver," *Computers and Fluids*, Vol. 92, pp. 281-292, 2014.

[27]Kirk, B., Stogner, R., Oliver, T., and Bauman, P., "Recent Advancements in Fully Implicit Numerical Methods for Hypersonic Reacting Flows," AIAA Paper No. 2013-2559, June 2013.

[28]Palmer, G., Barnhardt, M., Kirk, B., Amar, A., Chen, Y.-K., and Mansour, N., "Coupled CFD-Ablation Response Model Simulations Using the libMesh Framework," AIAA Paper No. 2014-2123, June 2014.

[29]Chen, Y.-K., Gokcen, T., "Implicit Coupling Approach for Simulation of Charring Carbon Ablators," *Journal of Spacecraft and Rockets*, Vol. 51, No. 3, pp. 779-788, 2014.

[30]Anderson, W.K. and Bonhaus, D.L., "An Implicit Upwind Algorithm for Computing Turbulent Flows on Unstructured Grids," *Computers and Fluids*, Vol. 23, No. 1, 1994, pp. 1-21.

[31]Johnston, C.O., Mazaheri, A., Gnoffo, P., Kleb, B., and Bose, D., "Radiative Heating Uncertainty for Hyperbolic Earth Entry, Part 1: Flight Simulation Modeling and Uncertainty," *Journal of Spacecraft and Rockets*, Vol. 50, No. 1, 2013, pp. 19-38.

[32]Tigelaar, D., Degges, M., Chuang, K., Hurwitz, F., Kuo, K., Scheiman, D., McCorkle, L., Quade, D., Vivod, S., and Splinter, S., "Synthesis and Characterization of Hyperbranched Polyazomethine Ablators for Space Exploration," *Journal of Thermophysics and Heat Transfer*, Vol. 28, No. 3, pp. 401-409, 2014.

[33]Qi, T., Bauschlicher, C., Lawson, J., Desai, T., and Reed, E., "Comparison of REAXFF, DFTB and DFT for Phenolic Pyrolysis. 1. Molecular Dynamics Simulations," *Journal of Physical Chemistry A,* Vol. 117, (2013), p. 11115.

[34]Bauschlicher, C., Qi, T., Reed, E., Lenfant, A., Lawson, J., and Desai, T., "Comparison of REAXFF, DFTB and DFT for Phenolic Pyrolysis. 2. Elementary Reaction Paths," *Journal of Physical Chemistry A,* Vol. 117, (2013), p. 11126.

[35]Monk, J., Haskins, J., Bauschlicher, C. and Lawson, J., "Molecular Dynamics Simulations of Crosslinked Phenolic Resins: Construction of Atomic Models", submitted to *Polymer*, 2014.

[36]Olds, A., Beck, R., Bose, D., White, J., Edquist, K., Hollis, B., Lindell, M., Cheatwood, F., Gsell, V., and Bowden, E., "IRVE-3 Post-Flight Reconstruction," AIAA Paper No. 2013-1390, March 2013.

[37]Hurwitz, F., Gallagher, M., Olin, T., Shave, M., Ittes, M., Olafson, K., Fields, M., Guo, H. and Rogers, R., "Optimization of Alumina and Aluminosilicate Aerogel Structure for High-Temperature Performance," *International Journal of Applied Glass Science*, Vol. 5, No. 3, pp. 276–286, 2014

[38]Tobin, S. and Dec, J., "Probabilistic Design Demonstration of a Flexible Thermal Protection System for a Hypersonic Inflatable Aerodynamic Decelerator," AIAA Paper No. 2015-xxxx, Jan 2015.

[39]Rossman, G. and Braun, R., "Material Property Testing of Flexible Thermal Protection Systems for Hypersonic Inflatable Aerodynamic Decelerator Thermal Response Modeling," AIAA Paper 2015-xxxx, Jan 2015.

[40]Goldman, B., Dowell, E., and Scott, R., "In-Flight Aeroelastic Stability of the Thermal Protection System on the NASA HIAD, Part II: Nonlinear Theory and Extended Aerodynamics," AIAA Paper No. 2015-xxxx, Jan 2015.

[41]Mazaheri, A., Gnoffo, P.A., Johnston, C.O., and Kleb, B., "LAURA Users Manual: 5.3-48528," NASA TM 216836, August 2010.

[42]Nompelis, I., Drayna, T.W., and Candler, G.V., "A Parallel Unstructured Implicit Solver for Reacting Flow Simulation," AIAA Paper 2005-4867, June 2005.

[43]Subbareddy, P.K. and Candler, G.V., "A Fully Discrete, Kinetic Energy Consistent Finite-Volume Scheme for Compressible Flows," *Journal of Computational Physics*, Vol. 228, pp. 1347-1364, 2009.

[44]Wheaton, B., Bartkowicz, M.D., Subbareddy, P.K., Schneider, S.P., and Candler, G.V., "Roughness-Induced Instabilities at Mach 6: A Combined Numerical and Experimental Study," AIAA Paper No. 2011-3248, June 2011.

[45]Brock, J.M., Subbareddy, P.K. and Candler, G.V., "Detached Eddy Simulations of Hypersonic Capsule Wake Flow," forthcoming in *AIAA Journal*.

[46]Stern, E.C., Gidzak, V.M., and Candler, G.V., "Estimation of Dynamic Stability Coefficients for Aerodynamic Decelerators Using CFD," AIAA Paper 2012-3225, June 2012.

[47]Candler, G.V, Subbareddy, P.K., and Nompelis, I., "Decoupled Implicit Method for Aerothermodynamics and Reacting Flows," *AIAA Journal*, Vol. 51, No. 5, pp.1245-1254, 2013.

[48]Trevino, L., and Candler, G.V., "Numerical Simulation of Regular Surface Patterns on Sublimating Ablative Materials," AIAA Paper No. 2015-xxxx, Jan. 2015.

[49]Candler, G., Johnson, H., Nompelis, I., Subbareddy, P., Gidzak, V., and Barnhardt, M., "Development of the US3D Code for Aerothermodynamics and Hypersonic Flow Simulations," AIAA Paper No. 2015-xxxx, Jan 2015.

[50]Gnoffo, P.A., "Updates to Multi-Dimensional Flux Reconstruction for Hypersonic Simulations on Tetrahedral Grids," AIAA Paper No. 2010-1271, Jan. 2010.

[51]Gnoffo, P.A., Wood, W.A., Kleb, W.L., Alter, S.J., and Glass, C.E., "A Tutorial for the Generic Gas Path in FUN3D," NASA TM-2014-XXXXX, Dec 2014.

[52]Gnoffo, P., "Global Series Solutions of Nonlinear Differential Equations with Shocks Using Walsh Functions," *Journal of Computational Physics*, Vol. 258, pp. 650-688, 2013.

[53]Cauchon, D.L., "Radiative Heating results from the FIRE II Flight Experiment at a Reentry Velocity of 11.4 Kilometers per Second," TM, NASA, July 1967.

[54]Wood, W. A., "Radiation Coupling with the FUN3D Unstructured-Grid CFD Code," AIAA Paper No. 2012-

2741, June 2012.

[55]Biedron, R.T., "FUN3D Manual: 12.4-69883," NASA TM 2014-218179, March 2014.

[56]Gnoffo, P., Wood, W., Kleb, B., Alter, S., Glass, C., Padilla, J., Hammond, D., and White, J., "Functional Equivalence Acceptance Testing of FUN3D for Entry, Descent and Landing Applications," AIAA Paper No. 2013-2558, June 2013.

[57]Gnoffo, P., "A Walsh Function Module Users Manual," NASA TM 2014-XXXX, April 2014.

[58]LeBeau, G., and Lumpkin III, F. "Application Highlights of the DSMC Analysis Code (DAC) Software for Simulating Rarefied Flows," *Computer Methods in Applied Mechanics and Engineering*, Vol. 191, 2001.

[59]Bird, G. A., *Molecular Dynamics and the Direct Simulation of Gas Flows* (Oxford University Press, Oxford, UK, 1994.

[60]Liechty, D., "State-to-State Internal Energy Relaxation Following the Quantum-Kinetic Model in DSMC," AIAA Paper No. 2013-2901, June 2013.

[61]Liechty, D., "Object Oriented / Data Oriented Design of a Direct Simulation Monte Carlo Algorithm," AIAA Paper No. 2014-2546, June 2014.

[62]Liechty, D. S., and Lewis, M. J. "Extension of the Quantum-Kinetic Model to Lunar and Mars Return Physics," *Physics of Fluids,* Vol. 26, 027106 (2014).

[63]http://www.nasa.gov/centers/ames/orgs/exploration-tech/entry-systems-div/east.html. Accessed November 16, 2014.

[64]Cruden, B. "Recent Progress in Entry Radiation Measurements in the NASA Ames Electric ARC Shock Tube Facility," Proceedings of the 5th International Workshop on Radiation of High Temperature Gases in Atmospheric Entry," Oct. 2012.

[65]Cruden, B., Brandis, A., and Prabhu, D., "Compositional Dependence of Radiance in $CO_2/N_2/Ar$ Systems," AIAA Paper No. 2013-2502, June 2013.

[66]Cruden, B., Brandis, A., White, T., and Bose, D., "Radiative Heating for MSL Entry: Verification of Simulations from Ground Test to Flight Data," AIAA Paper No. 2015-xxxx, Jan 2015.

[67]Cruden, B. A., Prabhu, D., Martinez, R., Le, H., Grinstead, J. H., and Bose, D., "Absolute Radiation Measurement in High Mass Venus and Mars Entry Conditions," AIAA Paper No. 2010-4508, June 2010.

[68]Johnston, C., Brandis, A., Panesi, M., Sutton, K., and Prabhu, D., "Shock Layer Radiation Modeling and Uncertainty for Mars Entry," AIAA-2012-2866, June 2012.

[69]Gazaric, M.J., Wright, M.J., Little, A., Cheatwood, F.M., Herath, J.A., Munk, M.M., Novak, F.J., and Martinez, E.R., "Overview of the MEDLI Project," IEEE Paper No. 2008-1510, Mar. 2008.

[70]Edquist, K., Hollis, B., Johnston, C., Bose, D., White, T., Mazhari, M., "Mars Science Laboratory Heat Shield Aerothermodynamics: Design and Reconstruction," *Journal of Spacecraft and Rockets*, Vol. 51, pp. 1106-1124, 2014.

[71]Karlgaard, C., Kutty, P., Shidner, J., Schoenenberger, M., and Munk, M., "Mars Entry Atmospheric Data System Trajectory Reconstruction Algorithms and Flight Results," AIAA Paper No. 2013-0028.

[72]Wray, A., "Improved Finite-Volume Method for Radiative Hydrodynamics", Seventh International Conference on Computational Fluid Dynamics (ICCFD7), Big Island, Hawaii, July 9-13, 2012.

[73]Brandis, A., Wray, A., Liu, Y., Schwenke, D., Carbon, D., Huo, W., and Johnston, C., "Validation of HyperRad for Earth Entries," AIAA Paper No. 2013-2777, June 2013.

[74]Park, C., "The Limits of Two-Temperature Model," AIAA Paper No 2010-0911, Jan. 2010.

[75]Y. Liu, W.M. Huo, A. Wray, and D. Carbon, "Electron Stark Broadening Database for Atomic N, O, and C lines," AIAA Paper No. 2012-2739, June 2012.

[76]H.P. Huber and G. Herzberg, "Molecular Spectra and Molecular Structure: IV. Constants of Diatomic Molecules", Van Nostrand Reinhold Co, New York, 1979.

[77]M. P. Deskevich, D. J. Nesbitt, and H.-J. Werner, J. Chem. Phys. **120**, 7281 (2004).

[78]D. W. Schwenke, Faraday Discuss., **109**, 321 (1998).

[79]Jaffe, R., Chaban, G. and Schwenke, D. "Theoretical Determination of High-Temperature Absorption Spectra for C_3 in the near-UV and VUV," AIAA Paper No. 2012-2743, June 2012.

[80]G. Monninger, M. Forderer, P. Gurtler, S. Kalhofer, S. Petersen, L. Nemes, P. G. Szalay, and W. Kratschmer, "Vacuum Ultraviolet Spectroscopy of the Carbon Molecule C_3 in Matrix Isolated State: Experiment and Theory", J. Phys. Chem. A, **106**, 5779-5788 (2002)

[81]J. P. Doering, and L. Goembel, Journal of Geophysical Research **97**, 4295 (1992).

[82]Huo, W., Liu, Y., Panesi, M., Wray, A., and Carbon, D., "Electron Impact Excitation Cross Sections for Modeling Non-Equilibrium Gas," AIAA Paper No. 2015-xxxx, Jan 2015.

[83]Panesi, M., Jaffe, R., Schwenke, D., Magin, T., "Rovibrational Internal Energy Transfer and Dissociation of

N2(1Sg+)-N(4S(u)) System in Hypersonic Flows," *Journal of Chemical Physics*, 2013 Jan 28;138(4):044312. doi: 10.1063/1.4774412.

[84]Panesi, M., Jaffe, R., and Schwenke, D., "Energy Transfer Study of N2-N2 Interactions by Using Rovibrational State-to-State Model," AIAA Paper No. 2013-3147, June 2013.

[85]Johnston, C. and Brandis, A., "Features of Afterbody Radiative Heating for Earth Entry," AIAA Paper No. 2014-2675, June 2014.

[86]Brandis, A. and Johnston, C., "Characterization of Stagnation Point Heat Flux for Earth Entry," AIAA Paper No. 2014-2374, June 2014.

[87]Brandis, A. "Validation of Shock Layer Radiation: Perspectives for Test Cases," Proceedings of the 5th International Workshop on Radiation of High Temperature Gases in Atmospheric Entry," Oct. 2012.

[88]Johnston, C., Brandis, A., and Bose, D., "Radiative Heating Uncertainty for Hyperbolic Earth Entry, Part 3: Comparisons with Electric Arc Shock Tube Measurements," *Journal of Spacecraft and Rockets*, Vol. 50, No. 1, pp. 48-55, 2013.

[89]Brandis, A. "Investigation of Nonequilibrium Radiation for Mars Entry," AIAA Paper 2013-1055, Jan. 2013.

[90] Brandis, A., Johnston, C., Cruden, B., Prabhu, D., Wray, A., Liu, Y., Schwenke D., and Bose, D., "Validation of CO 4th Positive Radiation for Mars Entry," *Journal of Quantitative Spectroscopy & Radiative Transfer*, 2013.

[91]Liu, Y., Panesi, M., Vinokur, M., and Clarke, P., "Microscopic Simulation and Macroscopic Modeling for Thermal and Chemical Nonequilibrium Gases," AIAA Paper No. 2013-3146, June 2013.

[92]Liu, Y., Panesi, M., Sahai, A., and Vinokur, M., "General Multi-Group Macroscopic Modeling for Thermochemical Nonequilibrium Gas Mixtures," AIAA Paper No. 2014-3204, June 2014.

[93]Johnston, C. and Brandis, A., "Modeling of Nonequilibrium CO Fourth Positive and CN Violet Emission in CO2-N2 Gases," *Journal of Quantitative Spectroscopy and Radiative Transfer*, Vol. 149, pp. 303-317, 2014.

[94]Johnston, C., "Influence of Radiative Absorption on Non-Boltzman Modeling for Mars Entry," *Journal of Thermophysics and Heat Transfer*, Vol. 28, No. 4, pp. 795-798, 2014.

[95]Panesi, M., Munafo, A., Magin, T., and Jaffe, R., "Nonequilibrium Shock Heated Nitrogen Flows Using a Rovibrational State-to-State Method," *Physical Review E*, Vol. 90, 013009, 2014.

[96]Wright, M.J., Olejniczak, J., Brown, J.L., Hornung, H.G., and Edquist, K.T., "Modeling of Shock Tunnel Heating Data on the Mars Science Laboratory Aeroshell," *Journal of Thermophysics and Heat Transfer*, Vol. 20, No. 4, 2006, pp. 641-651.

[97]MacLean, M. and Holden, M., "Numerical Assessment of Data in Catalytic and Transitional Flows for Martian Entry," AIAA Paper No. 2006-2946, June 2006.

[98]Hollis, B. and Prabhu. D., "Assessment of Laminar, Convective Aeroheating Prediction Uncertainties for Mars-Entry Vehicles," *Journal of Spacecraft and Rockets*, Vol. 50, No. 1 (2013), pp. 56-68.

[99]MacLean, M., Dufrene, A., and Holden, M., "Spherical Capsule Heating in High Enthalpy Carbon Dioxide in LENS-XX Expansion Tunnel," AIAA Paper No. 2013-0906, Jan. 2013.

[100]MacLean, M., Dufrene, A., Carr, Z., Parker, R., Holden, M., and Hollis, B., "Measurements and Analysis of Mars Entry, Descent and Landing Aerothermodynamics at Flight Duplicated Enthalpies in LENS-XX Expansion Tunnel," AIAA Paper No. 2015-xxxx, Jan 2015.

[101]Sharma, M., Swantek, A., Flaherty, W., Austin, J., Doraiswamy, S. and Candler, G., "Experimental and Numerical Investigation of Hypervelocity Carbon Dioxide Flow over Blunt Bodies," *Journal of Thermophysics and Heat Transfer*, Vol. 24, pp. 673-683, 2010.

[102]Sharma, M., Austin, J., Glumac, N., Swantek, A., and Flaherty, W., "Expansion Tube Investigation of Shock Standoff Distances in High Enthalpy CO_2 Flow Over Blunt Bodies," AIAA Paper No. 2010-1566, 2010.

[103]Sharma, M., Swantek, A., Flaherty, W., Austin, J., Doraiswamy, S. and Candler, G., "Evaluation of Hypervelocity Carbon Dioxide Blunt Body Experiments in an Expansion Tube Facility," AIAA Paper No. 2011-0136, 2011.

[104]Dirling, R.B., "A Method for Computing Roughwall Heat Transfer Rates on Reentry Nosetips," AIAA Paper No. 733-0763, July 1973.

[105]Reda, D., Wilder, M., and Prabhu, D., "Transition Experiments on Blunt Cones with Distributed Roughness in Hypersonic Flight," *Journal of Spacecraft and Rockets*, Vol. 50, No. 3, pp. 504-508, 2013.

[106]Wilder, M., Reda, D., and Prabhu, D., "Effects of Distributed Surface Roughness on Turbulent Heat Transfer Augmentation Measured in Hypersonic Free Flight," AIAA Paper No. 2014-0512, Jan. 2014.

[107]Wilder, M., Reda, D., and Prabhu, D., "Transition Experiments on Blunt Bodies with Distributed Roughness in Hypersonic Free Flight in Carbon Dioxide," AIAA Paper No. 2015-xxxx, Jan 2015.

[108]Reda, D., Wilder, M., and Prabhu, D., "Transition Experiments on Blunt Bodies with Isolated Roughness Elements in Hypersonic Free Flight," *Journal of Spacecraft and Rockets*, Vol. 47, No. 5, 2010, pp. 828–835.

[109]Wilder, M.C., Bogdanoff, D. W., and Cornelison, C. J., "Hypersonic Testing Capabilities at the NASA Ames Ballistic Ranges," AIAA Paper No. 2015-xxxx, Jan. 2015.

[110]Wool, M. R., "Final Summary Report Passive Nosetip Technology (PANT) Program," Aerotherm Report 75-159, June 1975.

[111]Reda, D. C., "Review and Synthesis of Roughness-Dominated Transition Correlations for Reentry Applications," *Journal of Spacecraft and Rockets*, Vol. 39, No. 2, 2002, pp. 161–167.

[112]Hollis, B., "Distributed Roughness Effects on Blunt Body Transition and Turbulent Heating," AIAA Paper No. 2014-0238, Jan. 2014.

[113]Bose, D., Brown J., Prabhu, D., Gnoffo, P., Johnston, C. and Hollis, B., "Uncertainty Assessment of Hypersonic Aerothermodynamics Prediction Capability," AIAA Paper No. 2011-3141, June 2001.

[114]Brown, J.L., "Hypersonic Shock Wave Impingement on Turbulent Boundary Layers: Computational Analysis and Uncertainty," *Journal of Spacecraft and Rockets*, Vol. 50, No. 1, pp. 96-123, 2013.

[115]Marvin, J., Brown, J., and Gnoffo, P., "Experimental Database with Baseline CFD Solutions: 2D and Axisymmetric Hypersonic Shock Wave / Turbulent Boundary Layer Interactions," NASA TM 2013-216604, Nov. 2013.

[116]Brown, J., "On Parametric Sensitivity of Reynolds Averaged Navier-Stokes SST Turbulence Model: 2D Hypersonic Shock Wave Boundary Layer Interactions," NASA TM 2014-218353, May 2014.

[117]Samareh, J. A., Maddock, R. W., and Winski, R. G., "An Integrated Tool for System Analysis of Sample Return Vehicles," 2012 IEEE Aerospace Conference Big Sky, Montana, March 2012.

[118]Samareh, J. A., Glaab, L., Winski, R. G., Maddock, R. W., Emmett, A. L., Munk, M. M., Agrawal, P., Sepka, S., Aliaga, J., Zarchi, K., Mangini, N., Perino, S., Bayandor, J., Liles, Charles, "Multi-Mission System Analysis for Planetary Entry (M-SAPE) Version 1," NASA/TM-2014-218507, Aug. 2014.